Opposite page:

AFM images showing the surface morphology of various organic/nanocrystal films. (A) Phase image of a partial monolayer of nanocrystals on top of organic thin film after phase segregation during spin-coating. Nanocrystal surface coverage is 21%. (B) Height image of a close-up of (A) showing both an island of nanocrystals as well as individual nanocrystals (QDs) on a flat organic background. (C) Phase image of a complete, hexagonally packed monolayer of nanocrystals phase segregated from the underlying organics. Grain boundaries between ordered domains of nanocrystals are observable.

Courtesy of S. Coe, J. Steckel, and W. Woo (M. Bawendi and V. Bulovic)

Sponsor:
NSF MRSEC Program, Universal Display Corporation, and the Institute for Soldier Nanotechnology (ISN)

Quantum Effect Devices

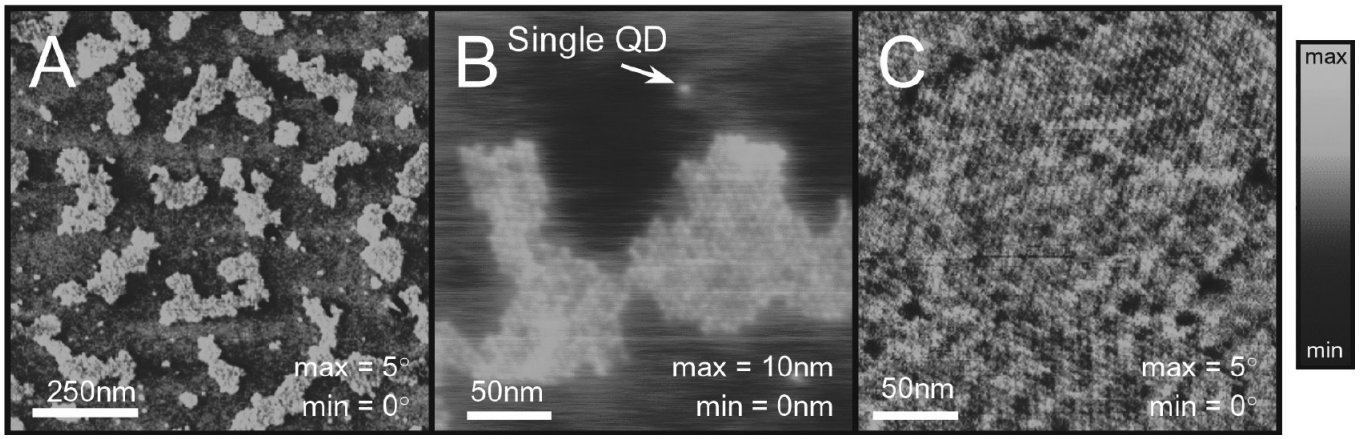

Quantum Effect Devices

- *On-Chip Oscillator Coupled to the Qubit: Design and Experiments to Reduce Decoherence*
- *Design of Coupled Qubit*
- *Thermal Activation Characterization of Qubits*
- *Type II Quantum Computing Using Superconducting Qubits*
- *Superconducting Persistent Current Qubits in Niobium*
- *Projective Measurement Scheme for Solid-State Qubits*
- *Improved Critical-Current-Density Uniformity of Nb Superconducting Fabrication Process by Using Anodization*
- *Superconducting Circuits and Quantum Computation*
- *Interaction Between Discrete Breathers and Other Non-Linear Modes in Josephson Arrays*
- *Vortex Ratchets*
- *Inorganic Quantum Dots in Organic Host Matrices for Efficient LEDs*
- *Fast On-Chip Control Circuitry*
- *Exciton Physics in Organic Optoelectronics*
- *Efficient Electrically Pumped Polariton Emission in a J-Aggregate OLED at Room Temperature*
- *An On-Chip Frequency-Domain Submillimeter-Wave Spectrometer*
- *Measurement of Qubit States with SQUID Inductance*

On-Chip Oscillator Coupled to the Qubit: Design and Experiments to Reduce Decoherence

Personnel

D. Crankshaw and B. Singh (T. Orlando)

Sponsorship

AFOSR and ARDA

The oscillator in Figure 1 is a simple, overdamped dc SQUID which acts as the on-chip oscillator which drives the qubit. This gives two parameters with which to control the frequency and amplitude of the oscillator: the bias current and the magnetic flux through the SQUID. In this design, the SQUID is placed on a ground plane to minimize any field bias from an external source, and direct injection supplies the flux by producing excess current along a portion of the SQUID loop. When a Josephson junction is voltage biased, its current oscillates at a frequency of $Vbias/\Phi_o$ with an amplitude of *Ic*. For a stable voltage bias, this looks like an independent ac current source. In this circuit, the junction is current biased, and its oscillating output produces fluctuations in the voltage across the junction. Thus the dc voltage, approximately equal to *IbiasRsh*, gives the fundamental frequency, while harmonics distort the signal. If the shunt is small, such that $Vbias >> Ic\,|\,Rsh + j\,\omega Lsh\,|$, the voltage oscillations are small relative to the dc voltage, and the higher harmonics become less of a problem. This allows us to model the junctions as independent sources (*I0* and *I1*) in parallel with the RCSJ model. A dc SQUID with a small self inductance behaves much like a single junction whose *Ic* can be controlled by the flux through its loop. The circuit model is shown in Figure 1. This is similar in concept to our previous work with Josephson array oscillators. The impedance seen by the qubit is given by placing the other elements of the circuit in parallel with the inductance. The maximum amplitude of the oscillating magnetic flux is at the resonance of the RLC circuit consisting of *Rc*, *Cc*, and *Lc*. In this case, the LC resonance occurs at 8.6 GHz. Directly on resonance, the SQUID produces high amplitude oscillations with a short dephasing time. Moving it off resonance lowers the amplitude but lengthens the dephasing time, as shown in Figure 2.

Table 1. SQUID oscillator parameters

Ic	Rn	Cj	Rsh	Lsh	Rc	Cc	Lc	Mc
260μA	7.3 Ω	2100fF	0.19 Ω	0.38 pH	0.73 Ω	4600fF	75 pH	0.6pH

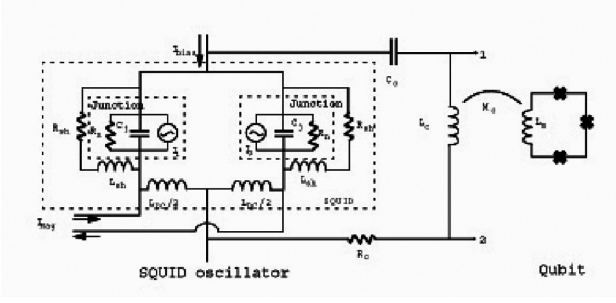

Fig 1: Circuit diagram of the SQUID oscillator coupled to the qubit. The SQUID contains two identical junctions, here represented as independent current sources and the RCSJ model, shunted by a resistor and inductor (Rsh and Lsh). A large superconducting loop (Lc) provides the coupling to the qubit. The capacitor, Cc, prevents the dc current from flowing through this line, and the resistance, Rc, damps the resonance. Zt, the impedance seen by the qubit, is the impedance across the inductor, Z12.

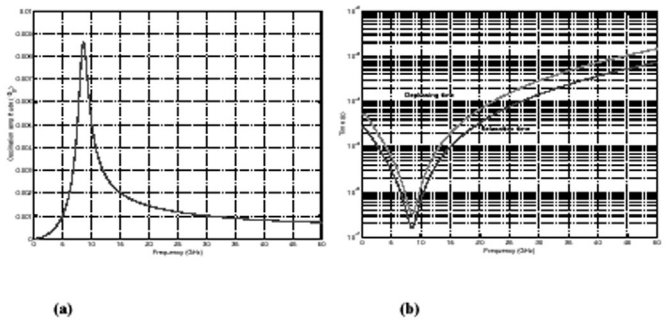

Fig. 2: Graphs showing the amplitude produced by the oscillator (a) and the decoherence times caused by the oscillator (b) as a function of frequency.

continued

continued

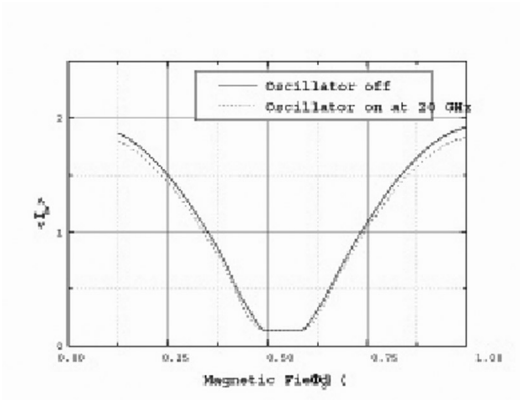

Fig. 3: This graph shows the switching current of the DC SQUID while the oscillator is off and while it is on. The current is clearly suppressed by turning the oscillator on. This oscillator has been fabricated and testing has begun. Although it is too early to comment on its effect on the qubit, it is clear that the oscillator is producing sufficient signal to suppress the current of the dc SQUID magnetometer used to measure the qubit's state, as shown in Figure 3.

Design of Coupled Qubit

Personnel

B. Singh, J. Habif, W. Kaminsky, and D. Berns
(T. Orlando and S. Lloyd)

Sponsorship

ARO and Hertz Fellowship

The main requirement for the coupled qubits is that the coupled qubit system have 4 distinguishable states corresponding to 4 properly spaced energy levels. Distinguishability here refers to the possibility of making a distinction between each of the 4 states by measurement. For a fully functioning 2-qubit quantum computer, it is necessary that the 4 qubit states that are functionally orthogonal be experimentally distinguishable. In the current design, the coupled qubits are actualized as two PC qubits weakly coupled by their mutual inductance. In the single qubit case, the DC measurement SQUID measures the state of the qubit through the flux induced by the qubit circulating current in the DC SQUID. The basic idea is unchanged for the coupled qubit system. In this case, there is one DC SQUID that measures the collective state of the coupled qubits through the total induced flux created by both qubits. For example the | 00> state could correspond to qubits 1 and 2 both having counterclockwise circulating current. In this case, the | 11> state would correspond to both qubits with clockwise circulating current. If the individual qubits were measurable with the DC SQUID, then the | 00> and | 11> states of the coupled qubit system should also be measurable because the total qubit flux induced on the DC SQUID is simply the sum of the individual qubit fluxes. The difficulty in measurement comes in differentiating the | 01> and | 10> states.

A difference in the measured flux from the | 01> and | 10> states can come from a difference in the mutual inductance between the individual qubits and the measurement SQUID and/or a difference in the magnitude of the circulating current for the two qubits. Currently, it is not practical to achieve the separation of flux states from adjusting mutual inductance values. Therefore, the approach has been to create two qubits with differing circulating current magnitudes. The magnitude of the circulating current is determined by the size of the junctions.

continued

Our analysis shows that there are 6 acceptable qubit parameter choices given the fabrication constraints for a single qubit. Since there are 2 qubits in the coupled qubit system, there are a total of 15 possible "distinct" coupled qubit combinations. Not all of these 15 possibilities are practical because some still require rather large qubit-SQUID coupling for distinguishability between the | 01> and | 10> states. The qubit-qubit and qubit-SQUID mutual inductance are parameters that can be varied through choices in geometry. As in the single qubit case, there are inherent tradeoffs in deciding on the appropriate size of the coupling. The need for properly spaced energy levels comes from the mode of operation of the qubit. The qubits will be rotated, be it individually or collectively, through RF radiation of the appropriate frequency. In the first round of experiments, the signal will come from an off-chip oscillator.

For the full functionality of the couple qubit system, it is required that there be 4 non-degenerate energy levels corresponding to the | 00, | 01, | 10, and | 11 states and that the 6 possible state transitions have sufficiently different resonant frequencies. If these conditions are met, then pulses with the appropriate linewidth would be able to do universal quantum computation on the 2-qubit system, including the "CNOT" operation. Following along the previous assumption that the coupled qubit system is accurately described as two individual qubits with weak mutual inductive coupling, it should be clear that the | 00> and | 11> states (corresponding to both qubits in the ground or excited states) should be well separated in energy. To meet the other requirements on the energy levels, the qubit-qubit mutual inductive energy needs to be sufficiently large, and the qubits need to have different junction sizes. The latter requirement is already necessitated by the measurement limitations. The former represents another tradeoff in the design, as there are problems if the coupling is too strong. Beyond the aforementioned desiderata, it is necessary that the magnitude of these resonant frequencies be practical for experiments. For the current fabrication run, there are 6 coupled qubit designs. An effort was made to span the acceptable parameter space for the tradeoffs mentioned above.

Thermal Activation Characterization of Qubits

Personnel

K. Segall, D. Nakada, D. Crankshaw, B. Singh, J. Lee, K. Berggren, N. Markovic and S. Valenzuela
(T. Orlando, L. Levitov, S. Lloyd in collaboration with M. Tinkham, Harvard)

Sponsorship

AFOSR grant funded under DURINT and ARDA

In our work, we have demonstrated two distinct measurable states of the qubit, have observed thermal activation between the two states, and have seen an effect where the measurement device acts on the qubit, an effect that we refer to as time-ordering of the measurements. The PC qubit is surrounded by a two-junction DC-SQUID magnetometer, which reads out the state of the PC qubit. The SQUID is highly underdamped, so the method of readout is to measure its switching current, which is sensitive to the total flux in its loop. A bias current Ib was ramped from zero to above the critical current of the SQUID, and the value of current at which the junction switched to the gap voltage was recorded for each measurement (See Figure 4bc). The repeat frequency of the bias current ramp was varied between 10 and 150 Hz. Typically, several hundred measurements were recorded, since the switching is a stochastic process. The experiments were performed in a pumped 3He refrigerator, at temperatures of 330 mK to 1.2 K. A magnetic field was applied perpendicular to the sample in order to flux bias the qubit near to one half a flux quantum in its loop.

The PC qubit biased near half a flux quantum can be approximated as a two-state system, where the states have equal and opposite circulating current. These two states will be labeled 0 and 1.

The circulating current in the qubit induces a magnetization into the SQUID loop equal to MIcirc, where M is the mutual inductance between the qubit and the SQUID and Icirc is the circulating current in the qubit. The two different circulating current states of the qubit cause two different switching currents in the SQUID. Without loss of generality, we can call 0 the state corresponding to the smaller switching current and 1 the state corresponding to the larger switching current. A central aspect of the measurement is that it takes a finite time to be completed. The current Ib(t) passes the smaller switching current at time t0 and the larger switching current at a later time t1 (See Fig. 1c). Measurement of state 0 occurs before measurement of state 1; this we refer to as time-ordering of the measurements. We call £n = (t1 – t0) the measurement time. Thermal activation of the system during time £n causes a distinct signature in the data and allows us to measure the thermal activation rate. The average switching current as a function of magnetic field is shown in Figure 5. The transfer function of the SQUID has been subtracted off, leaving only the magnetization signal due to the qubit. At low magnetic fields (to the left in Figure 5), the system is found only in the 0 state, corresponding to the lower switching current. As the magnetic field is increased, the system probability is gradually modulated until it is found completely in the 1 state, corresponding to the larger switching current. Focusing on the point in flux where the two states are equally likely, one can see that it is formed from a bimodal switching distribution, with the two peaks corresponding to the two different qubit states.

In Figure 5 we also show the best fit for each curve from our model. The same fitting parameters are used in both cases, with only the temperature allowed to vary. The 0.62 K curve has moved in flux relative to the 0.33 K curve, as expected. The theory predicts both the curve's shape and its relative position in flux. We use this agreement to fit the parameters of our system. There are three fitting parameters for the model to fit the data: EJ, α and Q. EJ is the Josephson energy for each of the two larger junctions in the three-junction qubit, which, for a given current density, is proportional to their physical size. The parameter α is the ratio of the smaller junction to the two larger ones, as previously mentioned. The damping factor Q is associated with thermal activation from the 1 to the 0 state in equation (3). The value of EJ which best fits the data is 4000 μeV. This corresponds to a size of about 0.52 μm x 0.52 μm for each of the two larger junctions. The values of α were found to be 0.58, corresponding to a smaller junction size of

continued

0.39 μm. These values are quite reasonable given the fabrication of our junctions. The larger junctions are lithographically 1 μm in length, while the smaller junctions are lithographically 0.9 μm; however, the fabrication process results in a sizing offset of between 0.4 and 0.55 μm, measured on similar structures.

The value of Q is found to be 1.2x106, with an uncertainty of about a factor of 3, given the sources of error in the measurement and the fitting. This value corresponds to a relaxation time of roughly α£s0 ~ 1 μs. Similar relaxation times have been measured in aluminum superconducting qubits and indicate possible long coherence times in the quantum regime. The value of 106 is consistent with a subgap resistance of 10 MΩ measured in similar junctions. The inferred relaxation time is also consistent with the calculated circuit impedance. This inferred value of Q is important for the long-term prospects of our qubits, as it indicates that it is possible to obtain very low dissipation in our structures.

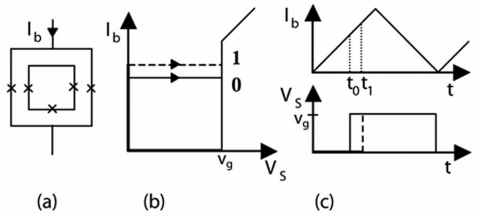

Fig. 4: (a) Schematic of the PC qubit surrounded by a DC SQUID. The X's represent junctions. (b) Schematic curve of the bias current (Ib) vs. the SQUID voltage (Vs) for the SQUID. At the switching point the SQUID voltage switches to the gap voltage vg. The 0 and 1 qubit states cause two different switching currents. (c) Timing of the current and voltage in the SQUID as the measurement proceeds. If the qubit is in state 0, Vs switches to vg at time t0; if the qubit is in state 1, Vs switches at time t1. The time difference t1-t0 forms a timescale for the measurement.

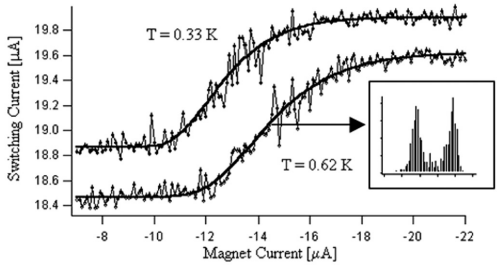

Fig. 5: Switching current versus magnetic field for device A for bath temperatures of T = 0.33 K and T = 0.62 K. The 0.33 K curve is intentionally displaced by 0.3 μA in the vertical direction for clarity. The model (equation (7)), with fitted temperature values of 0.38 K and 0.66 K, fits the data well, describing accurately the dependence of both the location of the midpoint of the transition and the shape of the transition on the device temperature. Inset shows a histogram for a flux bias where the system is found with equal probability in either state. The distribution is bimodal, showing the two states clearly.

Type II Quantum Computing Using Superconducting Qubits

Personnel

T. P. Orlando in collaboration with D. Berns, K. K. Berggren and J. Sage, Lincoln Laboratory, and J. Yepez, Air Force Laboratories)

Sponsorship

AFOSR funded under the Department of Defense and Defense University Research Initiative on Nanotechnology (DURINT)

Most algorithms designed for quantum computers will not best their classical counterparts until they are implemented with thousands of qubits. By all measures, this technology is far in the future. On the other hand, the Factorized Quantum Lattice-Gas Algorithm (FQLGA) can be implemented on a type II quantum computer, where its speedups are realizable with qubits numbering only in the teens. The FQLGA uses a type II architecture, where an array of nodes, each node with only a small number of coherently coupled qubits, is connected classically (incoherently). It is the small number of coupled qubits that will allow this algorithm to be of the first useful quantum algorithms ever implemented.

The algorithm is the quantum mechanical version of the classical lattice-gas algorithm, which can simulate many fluid dynamic equations and conditions with unconditional stability. This algorithm was developed in the 1980's and has been a popular fluid dynamic simulation model ever since. It is a bottom-up model where the microdynamics are governed by only three sets of rules, unrelated to the specific microscopic interactions of the system. The quantum algorithm has all the properties of the classical algorithm but with an exponential speedup in running time.

We have been looking into the feasibility of implementing this algorithm with our superconducting qubits, with long-term plans of constructing a simple type II quantum computer. We currently have a chip scheme to simulate the one dimensional diffusion equation, the simplest fluid dynamics to simulate with this algorithm. The requirements are only two coupled qubits per node, state preparation of each qubit, only one $\pi/2$ pulse, and subsequent measurement. This can be accomplished with two PC qubits inductively coupled, each with a flux bias line next to it (initialization), and each with a squid around it (measurement), with a tunable (frequency and amplitude) oscillator on-chip next to the two qubits (transformation). All classical streaming will, at first, be done off-chip.

Superconducting Persistent Current Qubits in Niobium

Personnel

Y. Yu, K. Segall, D. Nakada, D. Crankshaw, B. Singh, J. Lee, B. Cord, K. Berggren (MIT), N. Markovic and S. Valenzuela (Harvard) (T. Orlando, L. Levitov, S. Lloyd in collaboration with M. Tinkham, Harvard)

Sponsorship

AFOSR, funded under the Department of Defense and Defense University Research Initiative on Nanotechnology (DURINT) and by ARDA

Quantum Computation is an exciting idea whose study combines the exploration of new physical principles with the development of a new technology. In these early stages of research, one would like to be able to accomplish the manipulation, control, and measurement of a single two-state quantum system while maintaining quantum coherence. This will require a coherent two-state system (a qubit) along with a method of control and measurement.

Superconducting quantum computing has the promise of an approach that could accomplish this in a manner that can be scaled to large numbers of qubits. We are studying the properties of a two-state system made from a niobium (Nb) superconducting loop, which can be incorporated on-chip with other superconducting circuits to perform the control and measurement. The devices we study are fabricated at Lincoln Laboratory, which uses a Nb-trilayer process for the superconducting elements and photolithography to define the circuit features. Our system is, thus, inherently scalable, but has the challenge of being able to demonstrate appreciable quantum coherence.

The particular device that we have studied so far is made from a loop of Nb interrupted by 3 Josephson junctions (See Figure 6a). The application of an external magnetic field to the loop induces a circulating current whose magnetic field either adds to (say circulating current in the clockwise direction) or opposes (counterclockwise) the applied magnetic field. When the applied field is near to one-half of a flux quantum, both the clockwise and counterclockwise current states are classically stable. The system behaves as a two-state system. The potential energy versus circulating current is a so-called double-well potential (See Figure 7), with the two minima representing the two states of equal and opposite circulating current.

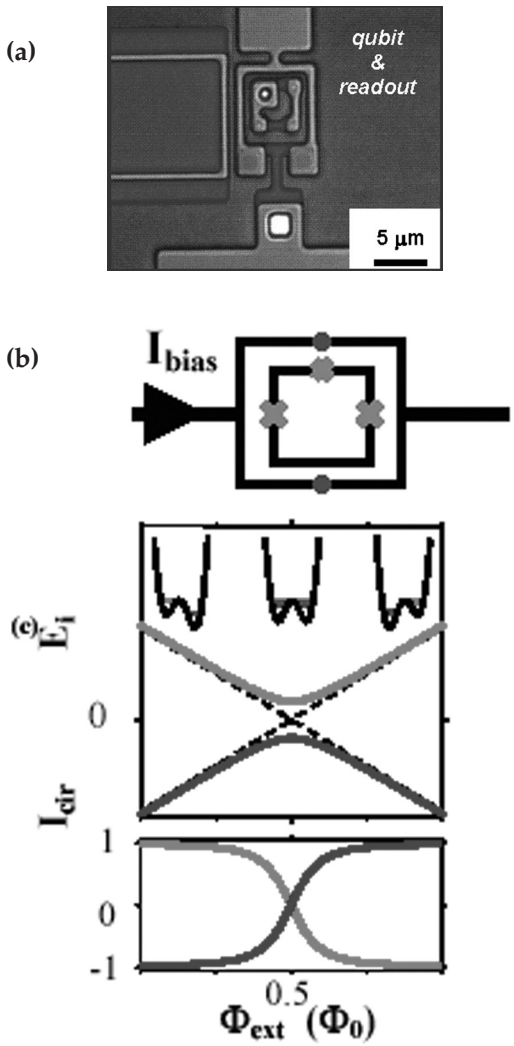

Fig. 6. (a) SEM image of the persistent current qubit (inner loop) surrounded by the measuring dc SQUID. (b) a schematic of the qubit and measuring SQUID, the x's mark the Josephson junctions. (c) The energy levels for the ground state (dark line) and the first excited state of the qubit versus applied flux. The double well potentials are shown schematically above.

continued

continued

The lower graph shows the circulating current in the qubit for both states as a function of applied flux. The units of flux are given in terms of the flux quantum.

Figure 6a shows a SEM image of the persistent current qubit (inner loop) and the measuring dc SQUID (outer) loop. The Josephson junctions appear as small "breaks" in the image. A schematic of the qubit and the measuring circuit is shown in Figure 6b, where the Josephson junctions are denoted by x's. The sample is fabricated at MIT's Lincoln Laboratory in niobium by photolithographic techniques on a trilayer of niobium-aluminum oxide-niobium wafer.

The energy levels of the ground state (dark line) and the first excited state (light line) are shown in Figure 6c near the applied magnetic field of 0.5 Φ_o in the qubit loop. Classically, the Josephson energy of the two states would be degenerate at this bias magnetic field and increase and decrease linearly from this bias field, as shown by the dotted line. Since the slope of the *E* versus magnetic field is the circulating current, we see that these two classical states have opposite circulating currents. However, quantum mechanically, the charging energy couples these two states and results in a energy level repulsion at Φ_{ext} = 0.5 £X0, so that there the system is in a linear superposition of the currents flowing in opposite directions. As the applied field is changed from below Φext = 0.5 Φ0 to above, we see that the circulating current goes from negative to zero at Φext = 0.5 Φ_o, to positive as shown in the lower graph of Figure 1c. This flux can be measured by the sensitive flux meter provided by the dc SQUID.

A SQUID magnetometer inductively coupled to the qubit can be used to measure the magnetic field caused by the circulating current and thus, determine the state of the qubit. The SQUID has a switching current which depends very sensitively on magnetic field. When the magnetic field from the qubit adds to the external field, we observe a smaller switching current; when it subtracts from the external field, we observe a smaller larger current. We measure the switching current by ramping up the bias current of the SQUID and recording the current at which it switches. Typically, a few hundred such measurements are taken. We have performed these measurements versus magnetic field, temperature, and SQUID ramping rate.

In the upper plot of Figure 7, we show the average switching current versus magnetic field for our qubit-SQUID system. The SQUID switching current depends linearly on the applied magnetic field. A step-like transition occurs when the circulating current in the qubit changes sign; hence, changing whether its magnetic field adds to or subtracts from the applied field. In Figure 6, the qubit field adds to the SQUID switching current at lower fields (< 3mG), but subtracts from it at higher fields (>3mG). Each point in the upper curve is an average of 1000 single switching current measurements. If we look at a histogram of the 1000 switching currents in the neighborhood of the transition, we discover that it represents a joint probability distribution.

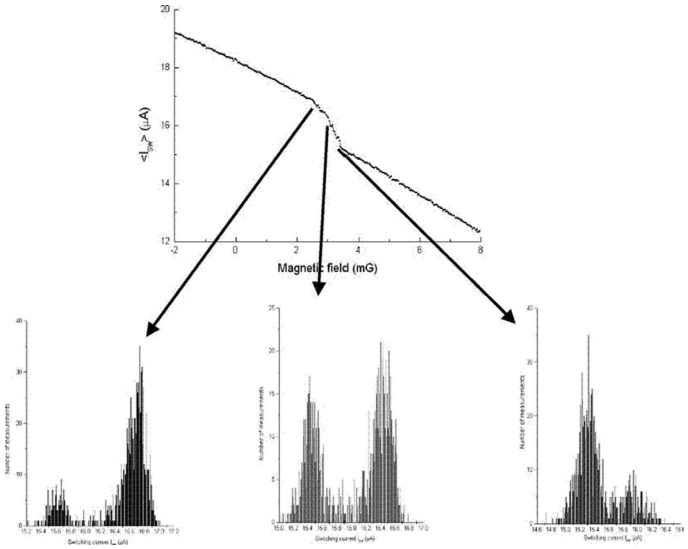

Fig. 7: Measurements of the switching current of the SQUID versus magnetic field.

continued

Two distinct switching currents representing the two states of the qubit can be clearly resolved. Changing the magnetic field alters the probability of being measured in one state or the other. In Figure 8, we show the potential energy for the system as we sweep through the transition. (We used a different assignment for "zero" field in Figure 8 than Figure 7, which is why the step occurs at a different magnetic field value). In the first part of the transition, the system has a higher probability of being measured in the left well, which corresponds to the circulating current state which adds to switching current of the SQUID. At the midpoint of the transition, the system is measured in both wells with equal probability. At higher fields the system has a larger probability of being measured in the right well. The mechanism for the system to move between the wells at these temperatures (>300 mK) is thermal activation. We have measured the system at lower temperatures, and there the mechanism is unclear. The focus of our future efforts is to determine if the mechanism changes to quantum mechanical tunneling at lower temperatures and how coherent the tunneling can be. If we are successful, that will be the first indication that superconducting quantum computers in Nb are possible.

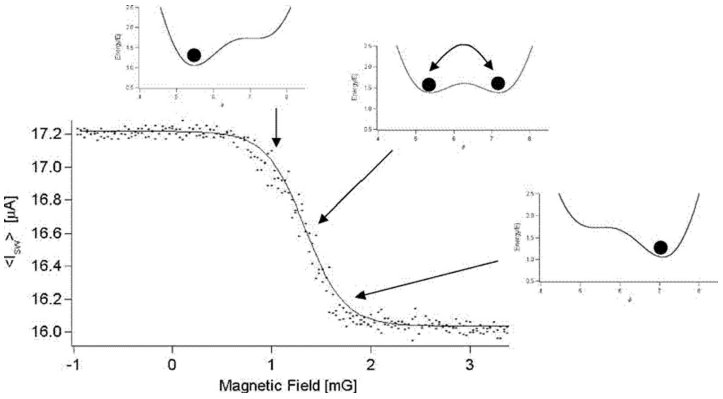

Fig. 8: Switching current versus magnetic field with the background field of the SQUID subtracted off.

Projective Measurement Scheme for Solid-State Qubits

Personnel

L. Tian (S. Lloyd and T. P. Orlando)

Sponsorship

Department of Defense University Research Initiative on Nanotechnology (DURINT)

Effective measurement for quantum bits is a crucial step in quantum computing. An ideal measurement of the qubit is a projective measurement that correlates each state of the quantum bit with a macroscopically resolvable state. In practice, it is often hard to design an experiment that can both projectively measure a solid-state qubit effectively and meanwhile, does **not** couple environmental noise to the qubit. Often in solid-state systems, the detector is fabricated onto the same chip as the qubit and couples with qubit all the time. On the one hand, noise should not be introduced to the qubit via the coupling with the detector. This requires that the detector is a quantum system well-isolated from the environment. On the other hand, to correlate the qubit states to macroscopically resolvable states of the detector, the detector should behave as a classical system that has strong interaction with the environment, and at the same time interacts with the qubit strongly. These two aspects contradict each other, hence, measurements on solid-state quantum bits are often limited by the trade-off between these two aspects. In the first experiment on the superconducting persistent-current qubit (pc-qubit), the detector is an under-damped dc SQUID that is well-isolated from the environment and behaves quantum mechanically. The detected quantity of the qubit, the self-induced flux, is small compared with the width of the detector's wave packet. As a result, the detector has very bad resolution in the qubit states. This is one of the major problems in the study of the flux-based persistent-current qubits. Various attempts have been made to solve the measurement problem. We present a new scheme in Figure 9 that effectively measures the pc-qubit by an on-chip detector in a "single-shot" measurement and does not induce extra noise to the qubit until the measurement is switched on. The idea is to make a switchable measurement (but a fixed detector) that only induces decoherence during the measurement. During regular qubit operation, although the qubit and the detector are coupled, the detector stays in its ground state and only induces an overall random phase to the qubit. The measurement process is then switched on by resonant microwave pulses. First, we maximally entangle the qubit coherently to a supplementary quantum system. Then, we measure the supplementary system to obtain the qubit's information.

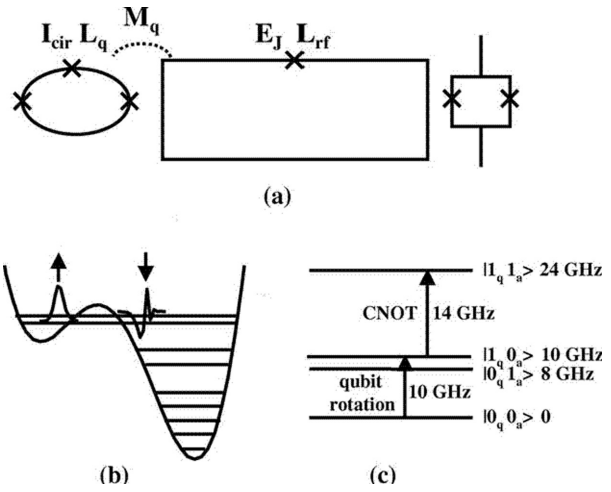

Fig. 9: (a). The circuit for the measurement scheme, from left to right: the qubit, the rf SQUID and the dc SQUID magnetometer. The pc-qubit couples with the rf SQUID via the mutual inductance M_q. (b). Energy levels of rf SQUID with its potential energy when biased at f_{rf} =0.4365 flux quantum. The effective two-level systems (ETLS) are labeled with arrows and their wave functions are shown. (c). The states of the interacting qubit and the rf SQUID. The energies are in units of GHz.

Improved Critical-Current-Density Uniformity of Nb Superconducting Fabrication Process by Using Anodization

Personnel

D. Nakada, K. K. Berggren, and E. Macedo (T. P. Orlando and B. Cord in collaboration with W. Oliver, Lincoln Laboratories)

Sponsorship

DOD, ARDA, ARO, and AFOSR

We developed an anodization technique for a Nb/Al/AlO*x*/Nb superconductive-electronics fabrication process that results in an improvement in critical-current-density *Jc* uniformity across a 150-mm-diameter wafer. The superconducting Josephson junctions studied were fabricated in a class-10 cleanroom facility at MIT Lincoln Laboratory. The Nb superconducting process uses optical projection lithography, chemical mechanical planarization of two oxide layers, a self-aligned via process, and dry Reactive Ion Etching (RIE) of the Nb and oxide layers. The most critical step in the fabrication process, however, is the definition of the tunnel junction. The junction consists of two Nb layers, the Base Electrode (B.E.) and Counter-Electrode (C.E.) separated by a thin AlO*x* barrier. Fig. 10a shows a cross-section of the Josephson junction region after RIE is performed on the counter-electrode. After RIE, the junction region could be vulnerable to chemical, plasma and/or other damage from subsequent processing steps; we, therefore, anodized the wafer to form a 50-nm-thick protective metal-oxide layer around the junction perimeter. Anodization is an electrolytic process in which the surface of a metal is converted to its oxide form; this metal oxide layer serves as a protective barrier to further ionic or electron flow. Figure 10b shows that after anodization the junction region is "sealed" from the outside environment by a thick NbO*x* layer. Anodization is useful in minimizing damage to the junction region. We also used Transmission Electron Microscopy (TEM) images to inspect the anodic film (Figure 11a, b and Figure 12).

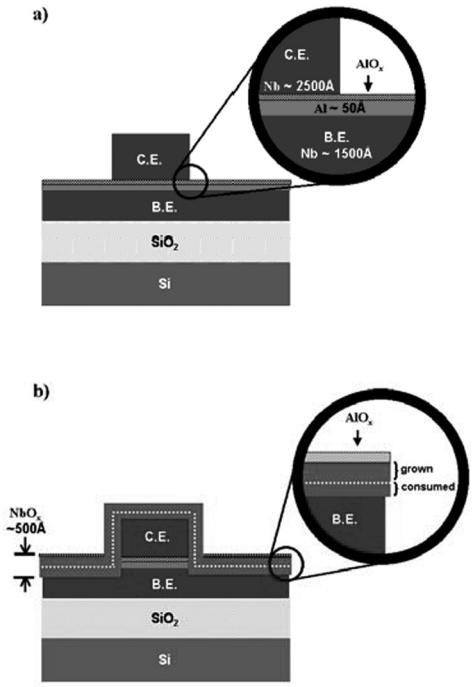

Fig. 10: a) Nb Josephson junction after Counter-Electrode (C.E.) etch but immediately prior to anodization. Inset shows thin AlOx barrier vulnerable to outside environment. b) Junction region after anodization. The surface of the counter and Base-Electrode (B.E.) is converted to a metal oxide layer approximately 500Å thick. The dotted line shows the original surface. Inset shows amount of anodic oxide grown and consumed. The anodic oxide causes the surface to swell up and out slightly during growth.

This work was sponsored by the Department of Defense under the Department of the Air Force contract number F19628-00-C-0002. Opinions, interpretations, conclusions and recommendations are those of the author and are not necessarily endorsed by the Department of Defense.

continued

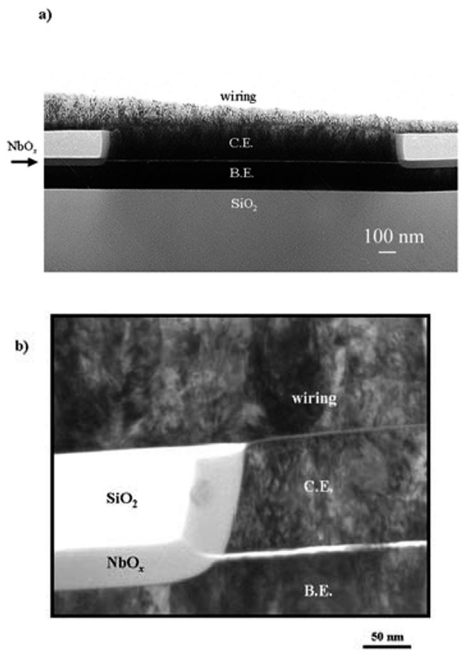

Fig.11: a) TEM image of an anodized junction showing clearly the sealing of the junction edge by NbOx. Note the clean interface between the counter-electrode and wiring layer where the NbOx has been removed by CMP. b) TEM image shows AlOx barrier within the NbOx layer. Critical current Ic measurements of Josephson junctions were performed at room temperature using specially designed test structures. We used an automatic probing station to determine the Ic values of junctions distributed across an entire wafer. We then compared the Jc uniformity of pairs of wafers, fabricated together, differing only in the presence or absence of the anodization step. The cross-wafer standard deviation of Jc was typically ~ 5% for anodized wafers but > 15% for unanodized wafers (Fig. 3). Overall, unanodized wafers had a factor of ~ 3 higher standard deviation compared to anodized wafers. A low variation in Jc results in a higher yield of device chips per wafer with the desired current density. As a result of the improved cross-wafer distribution, the cross-chip uniformity is greatly improved as well; typically < 1% for anodized chips. Control of Jc is important for all applications of superconductive electronics including quantum computation and rapid single-flux quantum (RSFQ) circuitry.

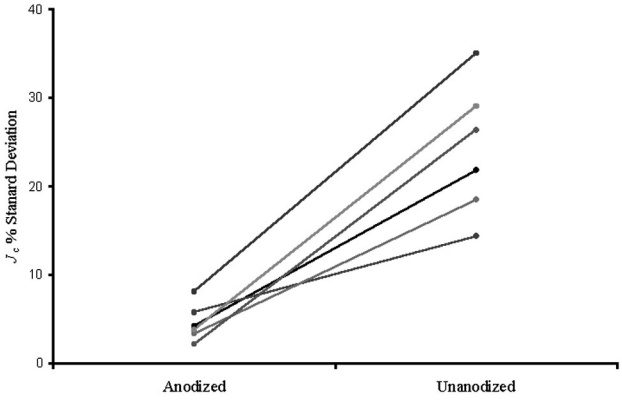

Fig. 12: Comparison of cross-wafer critical-current-density standard deviation of anodized/unanodized wafer pairs. The wafers shown have Jc values ranging between 102A/cm2 and 103A/cm2. Lines connect data points on wafers whose trilayers were deposited together.

Superconducting Circuits and Quantum Computation

Personnel

D. S. Crankshaw, D. Nakada, L. Tian, J. Lee, B. Singh, D. Berns, W. Kaminsky, B. Cord, M. Kota, A. Cough, Y. Yu, and K. J. Segall (T. P. Orlando, L. Levitov, S. Lloyd, J. E. Mooij in collaboration with J. Mazo, F. Falo, (University of Zarragossa), K. K. Berggren, W. Oliver (Lincoln Laboratories), M. Tinkham, N. Markovic, S. Valenzuela, (Harvard University), M. Feldman, M. Bocko, J. Habif, (University of Rochester, and E. Trais (Cadence, Inc))

Superconducting circuits are being used as components for quantum computing and as model systems for non-linear dynamics. Quantum computers are devices that store information on quantum variables and process that information by making those variables interact in a way that preserves quantum coherence. Typically, these variables consist of two quantum states, and the quantum device is called a quantum bit or qubit. Superconducting quantum circuits have been proposed as qubits, in which circulating currents of opposite polarity characterize the two quantum states. The goal of the present research is to use superconducting quantum circuits to perform the measurement process, to model the sources of decoherence, and to develop scalable algorithms. A particularly promising feature of using superconducting technology is the potential of developing high-speed, on-chip control circuitry with classical, high-speed superconducting electronics. The picosecond time scales of this electronics means that the superconducting qubits can be controlled rapidly on the time scale, and the qubits remain phasecoherent.

Superconducting circuits are also model systems for collections of coupled classical non-linear oscillators. Recently, we have demonstrated a ratchet potential using arrays of Josephson junctions as well as the existence of a novel non-linear mode, known as a discrete breather. In addition to their classical behavior, as the circuits are made smaller and with less damping, these non-linear circuits will go from the classical to the quantum regime. In this way, we can study the classical-to-quantum transition of non-linear systems.

Interaction Between Discrete Breathers and Other Non-Linear Modes in Josephson Arrays

Personnel

K. Segall and J. J. Mazo (T. P. Orlando)

Sponsorship

NSF and Fulbright/MEC Fellowship

Linear models of crystals have played a fundamental role in developing a physical understanding of the solid state. However, many phenomena are unexplained until one considers non-linear interactions. One particularly interesting phenomena is that of *discrete breathers*, which are time periodic, spatially localized modes. In a crystal, a discrete breather is localized in that a few atoms are vibrating while the neighboring atoms stay still. Josephson junctions are a solid state realization of non-linear oscillators, and they can experimentally be coupled in various ways using standard lithographic fabrication techniques. In Figures 13A and 13B, we show a regular array of Josephson junctions, denoted by x's, which are driven by a uniform current (driving current not shown). Each junction is governed by equations isomorphic to a damped pedulum; the phase of the pendula is equivalent to the superconducting phase difference across the junction. A discrete breather is shown in 13B, where a few of the junctions have their phases rotating in time while the others do not. Experimentally, a rotating phase corresponds to a net DC voltage, which can be easily measured. Breathers in Josephson arrays have been studied in previous work in our group here at MIT.

In Figure 13A, we demonstrate another kind of non-linear mode, a *moving vortex*. This is mathematically equivalent to a kink or solitonic mode. Vortices in Josephson arrays carry a quantum of magnetic flux and have been studied extensively in superconducting systems. A vortex corresponds to a 2π phase shift in the phases of the vertical juntions in the ladder; when a uniform current is applied, the vortex moves down the ladder. As the vortex passes a given junction, it causes its phase to undergo a rotation and thus create a voltage. This is indicated by the time sequence shown in Figure 13A. Our work is aimed at studying the interaction of discrete breathers with other kinds of non-linear modes, like a moving vortex. Such questions are of fundamental importance for the Non-linear Dynamics community. In Figure 14, we show a mathematical simulation of a

continued

collision between a vortex and a breather. The vertical axis is the junction number in the array; the array in the simulation has 60 junctions. The horizontal axis is time. The color indicates the junction voltage or rotation speed, with blue indicating low voltage and red indicating high voltage. Initially, there is a breather located about junction 10 and a vortex located in junction 45. As time proceeds, the vortex moves toward the breather and eventually collides with it. The result of the collision is that the breather acts as a pinning center for the vortex. As time proceeds further, (not shown) the vortex will eventually depin and cause the breather to decay into a different mode. We have also seen other collision scenarios in our simulations, such as ones where the breather is destroyed or where the breather pins a train of moving vortices. We are also looking for such behavior experimentally, with fabricated junction arrays and DC electronics.

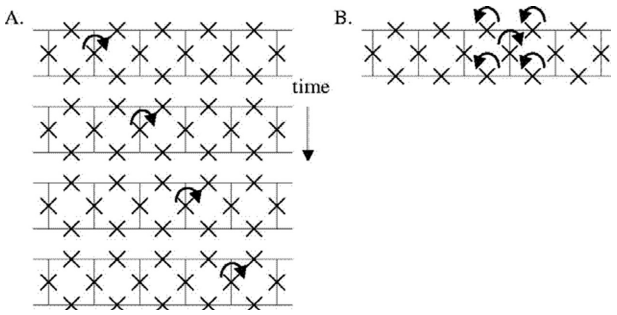

Fig. 13: Representation of two different non-linear modes in a Josephson Ladder: (a) Moving vortex: The vortex causes the phase of a junction to rotate as it passes by. (b) Discrete breather: A few junctions have their phases continually rotating while the neighboring ones do not.

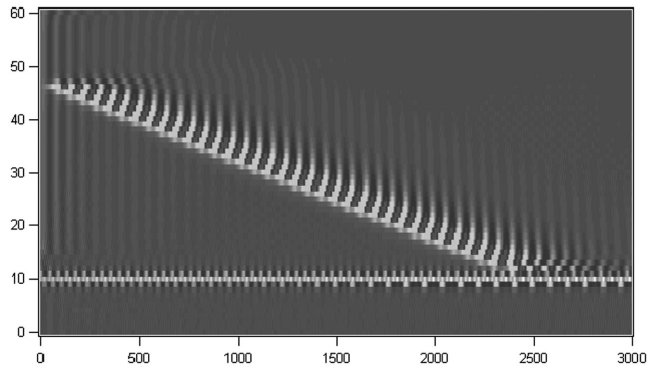

Fig. 14: Interaction of a breather with a moving vortex. Time (in arbitrary units) is on the horizonal axis, the junction number is on the vertical axis, and the color indicates the junction voltage (red=high, blue=low). The vortex starts in junction 45 and moves toward the breather, which is in junction 10. The vortex collides with the breather and is pinned by it, with the breather surviving at later times.

Vortex Ratchets

Personnel
K. Segall and J. J. Mazo (T. P. Orlando)

Sponsorship
NSF and Fulbright/MEC Fellowship

The concepts of a *ratchet* and of the *ratchet effect* have received attention in recent years in a wide variety of fields. Simply put a ratchet is formed by a particle in a potential which is asymmetric, i.e. it lacks reflection symmetry. An example is the potential shown in Figure 15, where the force to move a particle trapped in the potential is larger in the left (minus) direction and smaller in the right (plus) direction. The ratchet effect is when net transport of the particle occurs in the absence of any gradients. The transport is driven by fluctuations. This can happen when the system is driven out of equilibrium, such as by an unbiased AC force or non-gaussian noise.

Ratchets are of fundamental importance in biological fields for study of dissipation and stochastic resonance, in mesoscopic systems, and in our case in superconducting Josephson systems. The key question is to study how the ratchet potential affects the transport of the particle. In our group, we study the ratchet effect in circular arrays of superconducting Josephson Junctions. In such arrays, magnetic vortices or kinks can be trapped inside and feel a force when the array is driven by an external current. The potential that the vortex feels is given by a combination of the junction sizes and the cell areas; by varying these in an asymmetric fashion, we can construct a ratchet potential for a vortex. The picture in Figure 15 is of one of our fabricated circular arrays; the potential shown in Figure 15 is the numerically calculated potential for a kink inside the array. We have verified the ratchet nature of the potential with DC transport measurements, as published in early 2000.

This work is now moving in the quantum direction: smaller junction arrays where quantum effects are important. A quantum ratchet will display new behavior as the temperature is lowered, as both the ratchet potential and quantum tunneling can contribute to the kink transport. We have designed and fabricated such arrays and are presently testing them. The experiment we conduct in these newer devices is to measure the switching current, which is the current that is required to cause the vortex to depin and the system to switch to a running mode or finite voltage state. In the mechanical analog, it represents the critical force to move the particle, and in a ratchet potential it is different in one direction than the other. For a classical ratchet, the direction with the lower critical force will always have the larger depinning rate. However, in a quantum ratchet the direction with the lower transition rate will depend on the temperature. A crossover in the preferred direction, the direction with the larger depinning rate, is the signature of possible quantum behavior. In Figure 16, we show the switching current as a function of temperature for the two directions. A crossover is clearly seen. We are in the process of doing further experiments and calculations to verify that we have truly made a quantum ratchet.

continued

continued

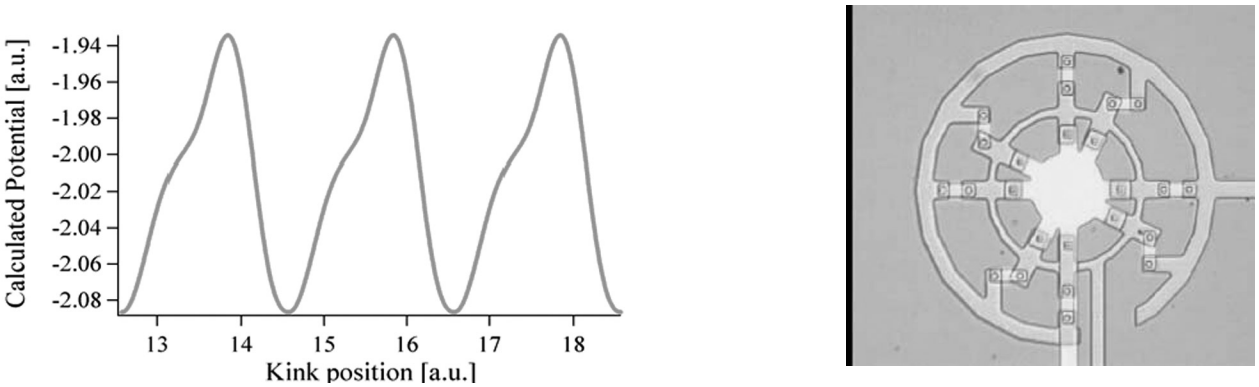

Fig.15: A ratchet potential and its realization in a Josephson array. The array has alternating junction sizes and plaquete areas to form the asymmetric potential for a vortex trapped inside the ring. The outer ring applies the current such that the vortex transport can be measured. The potential is numerically calculated for the array parameters.

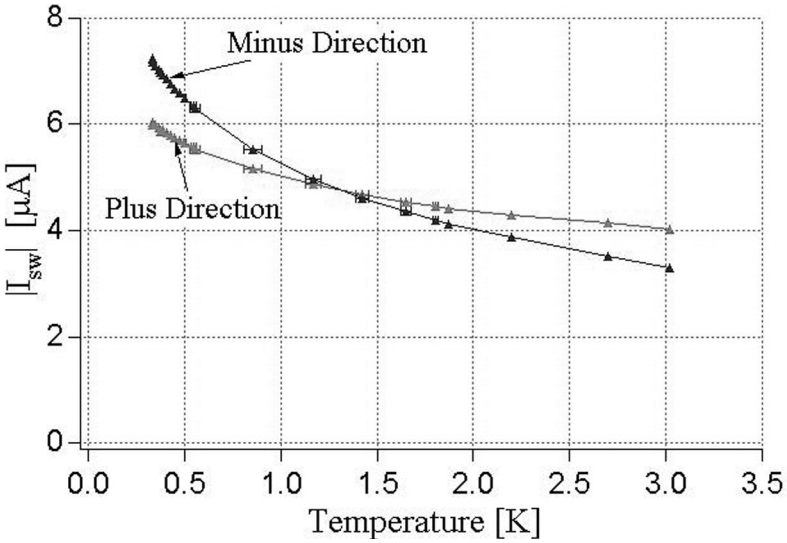

Fig. 16: Switching current for the plus and minus direction of a circular, 1-D Josephson array fabricated in the quantum regime. The switching current is a measure of the depinning rate in each direction. The crossover indicates that the preferred direction changes as a function of temperature. This is a possible signature of quantum effects.

Inorganic Quantum Dots in Organic Host Matrices for Efficient LEDs

Personnel

S. Coe, J. Steckel, and W. Woo (M. Bawendi and V. Bulovic)

Sponsorship

NSF MRSEC Program, Universal Display Corporation, and the Institute for Soldier Nanotechnology (ISN)

We recently demonstrated the first efficient hybrid organic/inorganic Light Emitting Devices (LEDs), with saturated color emission, whose performance reaches that of the all-organic LED technology (See Figure 17) [Coe *et al.*, Nature 420, 800 (2002)]. The hybrid LEDs are large-area, efficient light emitters consisting of luminescent inorganic nanocrystals (quantum dots) embedded in organic LED structures. They represent a completely new technology platform for development of the flat-panel displays and the flat-panel lighting. Their greatest benefit is in the ease of tuning their saturated emission color across the visible spectrum (by changing the size of the nanocrystal), and in their potentially longer operating lifetimes as compared to the all-organic LEDs.

(a) CdSe Quantum Dots

Nanocrystal Quantum Dots (QDs) are semiconductor nanoparticles that are chemically synthesized using simple benchtop techniques. Their sizes can be precisely controlled in a range from 1 to 10 nanometers. Electrons and holes are delocalized in QDs in states that are reminiscent of atomic wavefunctions. The energy of these states is strongly size-dependent: emission from CdSe QDs can be tuned across the entire visible spectrum by changing the size of the nanocrystals. Nanocrystal QDs can be synthesized with narrow size distributions so that the bandwidth of the emission can be < 30 nm. The dots are grown in organic solvents. Their surface is covered with a ligand shell that can be easily exchanged, giving the dots the potential for broad chemical and electronic flexibility (See Figure 17). The combination of broad spectral tunability and chemical flexibility make nanocrystal QDs ideal chromophores for opto-electronic applications in organic/inorganic hybrid structures such as QD-LEDs.

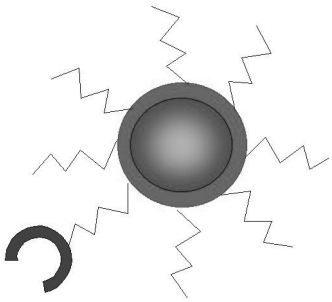

Fig. 17: Schematic of a QD showing an optically active core, a protective inorganic shell, an organic ligand shell, with one of the ligands functionalized.

QDs have unique advantages over other classes of common (small molecule or inorganic phosphor) chromophores. The emission wavelength of a QD depends on its size, and can be controlled by varying the diameter of the particle. The excitation band is very broad, requiring only that the excitation light, or energy tranfered excitations be above the band gap of the semiconductor; and it is independent of the emission, so that the same energy can be used to excite QDs with different emissions. A size series of QDs represents a family of fluorophores with different emissions that can be excited with the same light source. Furthermore, QDs are significantly less susceptible to photobleaching than dye molecules, making them ideal candidates as the chromophore in organic/inorganic hybrid structures. The energy level structure of QDs also differs substantially from most organic chromophores. The emission from QDs is from a lowest transition that is thought to be partly spin forbidden, leading to long (10-100 nsec) emission lifetimes at room temperature (and microseconds at cryogenic temperatures). The density of states above this emissive state becomes dense with both spin allowed (equivalent to singlet states of organics) and spin forbidden states (equivalent to the triplet states in organics). This high density of states should make QDs ideal in both Förster and Dexter transfer schemes of coupling excitons from organics to the QD.

continued

continued

(b) Performance of Layered Structures Containing QDs
The demonstration of quantum dot LEDs (QD-LEDs) is a direct result of a cross-disciplinary merge of the nanocrystal chemistry of Prof. Bawendi's lab and Prof. Bulović's lab expertise in the development of active organic optoelectronics. The devices incorporate CdSe nanocrystals in a molecular organic host via spin-on deposition of solvated materials. Spin-casting results in the formation of an organic/nanocrystal bilayer film due to the alkyl/phenyl phase segregation, where by alkyl-coated nanocrystals form a densely packed single monolayer on top of the conjugated organic film (See Figure 17 and device cross section in Figure 20). The devices are completed by thermally evaporating thin organic films and a metal cathode on top of the organic/nanocrystal layers. These first devices operate with a quantum efficiency of 0.4%; they have a saturated color, and brightness of 1500 cd/m^2 at current density of 120 mA/cm^2, corresponding to luminescence efficiency of 1.25 cd/A, as compared to the best previous results for nanocrystal-LEDs of 600 cd/m^2 at 1 A/cm^2, corresponding to 0.06 cd/A.

The remarkable 20-fold improvement in the electroluminescence efficiency of our QD-LEDs is attributed to the optimized device structures and improved photoluminescence efficiency and chemical stability of nanocrystals. The technologically innovative step of generating the self-assembled nanocrystal monolayer through phase segregation allows us to position the nanocrystals in the recombination zone of the multilayer active organic EL device. Their confinement to the device active region maximizes the efficiency of nanocrystal usage. Furthermore, the use of alkane/phenyl phase segregation to create spin-cast heterostructures provides a new general method for the fabrication of organic or hybrid devices.

The layer design of our QD-LEDs deliberately isolates the role of QDs in the luminescence processes from their participation in charge conduction by containing only a single monolayer of QDs within the structure. The organic layers transport charge carriers to the vicinity of the QD monolayer from which the luminescence originates. This is in contrast to previous studies that utilized QD multilayer films, on the order of 10-20 layers thick, which had the dual function of both transporting electrons and serving as the emissive layer. Poor conduction through these QD multilayers lead to an injected charge imbalance, and consequently, luminescence efficiency of these early devices never exceeded 0.10 cd/A. Furthermore, a high density of pinhole defects in QD multilayers resulted in low device yields and inconsistent device performance. These technological shortcomings are avoided in our new structures that use only a single monolayer of QDs as the emissive layer. High device yields and consistent LED performance are standard for our devices.

(c) Charge Transport and Energy Transfer in Hybrid Structures
Generation of excitons on QDs in our LED structures occurs via two parallel processes: direct charge injection and exciton energy transfer from organic molecules (See Figure 20). For direct charge injection, electrons may be trapped at the QDs due to the relative energy alignment of the Lowest Unoccupied Molecular Orbital (LUMO) levels of the electron transporting organic layer (Alq_3) and the QDs (see the energy diagram in Figure 19). For these charged QDs the barrier to hole injection from the hole transporting organic (TPD) is reduced. Upon acceptance of holes from TPD, excitons form on the QDs and can subsequently recombine radiatively. Alternatively, excitons can be formed on organic molecules that are near grain boun-daries, interstitial spaces, and voids in the single QD mono-layer. These excitons can then energy transfer to the lower energy QD sites, where they recombine radiatively.

In this program, we are studying the relative importance of the direct charge injection in comparison to energy transfer

continued

continued

processes for exciton generation on QDs. For example, by increasing the thickness of the shell structure of the dot, we can preferentially inhibit the short range charge tunneling processes into the dot (See Figure 19). The longer range (up to 50 Å transfer radius) Förster energy transfer is still be able to take place. Similarly, we are able to evaluate relative importance of Auger processes in quenching the emission of the QDs.

The quantum dot structure strongly affects the QD-LED performance. For example, the semi-log plot of the spectral emission intensity as a function of drive current is shown in Figure 21 for (a) ZnS coated CdSe nanodots and (b) uncoated CdSe nano-dots. Synthetic step for the coating process is indicated in the inset. In both cases, dots are surrounded by organic ligands to facilitate solvation in the organic solvent during the spin-on process. Both plots in Figure 20 show a strong luminescence peak at 570 nm corresponding to the nanodots emission, but we also observe a long luminescence tail form 700 to 950 nm. This emission is due to the luminescence form deep traps (mid-gap states) caused by dangling bonds on the surface of the nanodots. Trap luminescence is very inefficient and is more pronounced in uncoated dots. This typically results in several-fold lower efficiency of uncoated devices as has been previously observed in the PL spectra of the nanodots. The progression of luminescence as a function of device current indicates that for the coated-nanodot devices (See Figure 21) (a), luminescence of deep traps stays constant as the luminescence form the nanodots increases with current. For uncoated-dot devices, deep trap luminescence rises with current together with the dot luminescence. This is as expected: the small number of defect levels in the coated-dot devices is first populated at lower currents, and then, the luminescence form the confined states of the dot can start as the current is increased. The number of defect states on uncoated dot devices is significantly larger and cannot be filled completely even at higher device currents, so its luminescence steadily increases with the increase in current.

We are also interested in tailoring exciton generation processes and exciton energy transfer under electrical pumping conditions in the hybrid thin films.

Electrically generated excitons in organic materials can be of either singlet and triplet type, with their ratio corresponding to their spin multiplicities. In contrast, excited states of QDs mix the spin-triplet and spin-singlet exciton characteristics. In other material systems, such mixed states facilitate capture of both singlet and triplet excitons on the lumophore. Rapid exciton recombination that follows can lead to nearly 100% internally quantum efficienct LEDs. It remains an open question as to whether or not analogously efficient exciton harvesting is possible in QD-LEDs.

The fundamental limits of QD-LED performance are different than those of all organic LEDs. The discrete energy structure of QDs gives rise to a narrow emission spectrum, which in our electroluminesent devices is as small as 32 nm at full-width-half-maximum (FWHM). In contrast, molecular organic LEDs have a typical FWHM of between 50 and 100 nm, although emission of some polymers and phosphorescent molecules was shown to be as narrow as 26 nm FWHM but with long, low energy tails. The vibrational structure of structurally flexible organics typically generates broad single molecule emission spectra at room temperature. The same is not true of the rigid, covalently bonded inorganic QD, for which single QD spectroscopy shows that the fundamental FWHM linewidth at room temperature is 14 nm with a symmetrical, gaussian shape. It is the combination of spectral diffusion and size distribution of QDs in a specific sample that yields further line broadening. However, it is reasonable to expect that current techniques in QD preparation and processing could yield QD-LED line widths that

continued

continued

are as narrow as 25 nm, a feat that has already been accomplished in solution. Such true color saturation would benefit applications where efficient production of narrowband light is desired. In particular, the creation of high luminous efficiency red and blue LEDs requires both high external quantum efficiency as well as narrowband emission, to prevent the bulk of emission from occurring in the infrared or ultraviolet, respectively, where our eyes have minimal response.

With the demonstrated improvement in the luminescent power efficiency of QD-LEDs, we still have not reached the fundamental limits of device performance in both quantum efficiency and color saturation. We expect that with our development of the new methods for growth of QD-films in vacuum, higher material purity will be obtained. Performance of such vacuum-grown QD-LEDs could match and potentially exceed that of conventional organic thin-film LEDs, resulting in durable, integratable, highly-efficient light sources of nano-scale thickness. By changing the diameter of the CdSe core from 22 to 65Å, the peak luminescence wavelength can be precisely tuned from l=470 nm to l=640 nm with a typical spectral full width at half of maximum of less than 35nm. Figure 22 shows the electroluminescence spectra of a series or visible and infra-red emitting QD-LEDs. Such broadly tunable, saturated color emission of quantum dots is unmatched by any class of organic chromophores. Furthermore, environmental stability of covalently bonded inorganic nanocrystals suggests that device lifetimes of hybrid-LEDs should match or exceed that of all-organic LEDs.

(d) QD Monolayer Formation via Material Phase Segregation

QD-LEDs demonstrate that sheets of single QD monolayers, square centimeters in size, can be employed in electrically active devices. This minimizes QD material use to the active device region. The material phase segregation that governs formation of the organic/QD spin-cast thin film bilayers is a general and, we expect, widely applicable fabrication process. The process is governed by the physical size and chemical character of the two solvated constituents; the organic molecules in our devices are small (~1 nm) and have aromatic character, while the QDs are large in comparison (>3 nm) and present a surface that consists of mostly alkane chains. In general, phase segregation is not limited to aromatic/aliphatic pairs, but governs the interaction between any pair of materials with disparate chemical functionality. To date, the phase segregation phenomenon has been observed in spin cast solutions of (CdSe)ZnS core-shell/TOPO capped QDs and PbSe/oleic acid capped QDs with both α-NPD and TPD in chloroform and chlorobenzene.

(e) Infra-Red QD-LEDs

We also demonstrate large area (mm^2 in size) infrared electroluminescent devices using colloidally grown PbSe quantum dots (QDs) in organic host materials (See Figure 23). By changing the QD size, the electroluminescence is tuned from 1.33 μm-1.56 μm with a full width at half maximum of <160 nm (< 0.11 eV). This represents only a portion of the accessible QD tuning range, as the lowest energy optical absorption peak of our PbSe solutions can be tuned from 1.1 eV (corresponding to wavelength λ = 1.1 μm and 2.6 nm diameter QDs) to 0.56 eV (λ = 2.2 μm, 9.5 nm diameter). Such large area emitters in the near infrared have been identified as technologically useful for chemical spectroscopy and sensing, night vision applications, and could be incorporated into an on-chip optoelectronic integrated circuit.

PbSe is a convenient choice for inorganic semiconductor QDs for NIR applications (λ > 1 μm), as the colloidal synthesis is reproducible and yields highly monodisperse nanocrystals. In addition, the exciton Bohr radius is large (46 nm), leading to strong confinement of QD excitons throughout the synthetically accessible range of 2 nm to >10 nm

continued

continued

(corresponding to absorption peaks $\lambda = 1.0\ \mu m$ (1.2 eV) to >2.4 μm (<0.5 eV), respectively). Figure 23(a) shows typical absorption and emission spectra for 5.0±0.5 nm diameter PbSe QDs, while Figure 22(b) depicts an ordered layer of 4.0±0.5 nm diameter QDs imaged by high resolution transmission electron microscopy, showing their highly crystalline structure in the inset. The NIR EL spectrum of QD-LEDs closely resembles the PL spectrum of the corresponding QD solution (see Figure 23(a)). The tunability of QD-LED emission as a function of the QD diameter is shown in Figure 21(a), with EL spectral peaks at 1.33, 1.42, 1.50, and 1.56 μm. The FWHM of all four devices is <160 nm (< 0.11 eV). The devices also have an emission peak at 530 nm (not shown) due to exciton recombination within the Alq_3 ETL (or 405 nm corresponding to TPD EL when BCP is used as the ETL). We note that the InGaAs photodiode array used to record all of these spectra has low detection efficiency for λ >1.6 μm, modifying the apparent shape of the 1.56 μm emission peak.

The electrical characteristics of all the QD-LEDs of this study are similar, with a linear (J) versus voltage (V) dependence for V<3 V, and power law dependence, $J \propto V^9$, when light is emitted. This is consistent with the properties of an Alq_3/TPD device, though the operating voltage is a few volts higher, possibly due to QD charge trapping or interface dipole realignment. The PbSe QD-LED NIR external quantum efficiency is measured to be 0.001%, using a Silicon wafer to filter out visible emission from organic EL. The visible emission originates from Alq_3 and TPD and has an external EL quantum efficiency of 0.1-0.3%. These QD-LEDs demonstrate the feasibility of generating controllably tunable λ >1.3 μm EL in a large area device, and give us a starting point in the creation of higher efficiency devices in the spectral range of 1.2 $\mu m < \lambda < 2.2\ \mu m$.

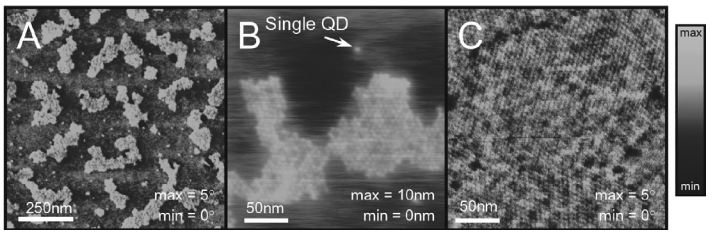

Fig. 18: AFM images showing the surface morphology of various organic/nanocrystal films. (A) Phase image of a partial monolayer of nanocrystals on top of organic thin film after phase segregation during spin-coating. Nanocrystal surface coverage is 21%. (B) Height image of a close-up of (A) showing both an island of nanocrystals as well as individual nanocrystals (QDs) on a flat organic background. (C) Phase image of a complete, hexagonally packed monolayer of nanocrystals phase segregated from the underlying organics. Grain boundaries between ordered domains of nanocrystals are observable.

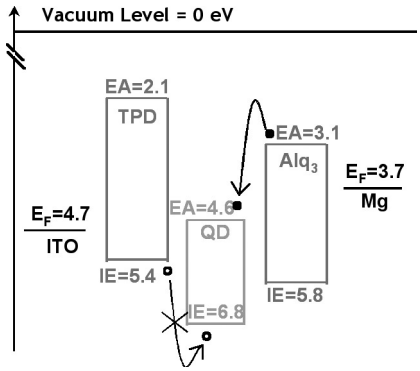

Fig. 19: Proposed energy level diagram of device in Fig. 18. Values for ionization energy (IE) of all materials except QDs are taken from photoemission spectroscopy measurements1. Electron affinity levels (EA) were then calculated using optical absorption data. QD levels shown are from calculated values

continued

continued

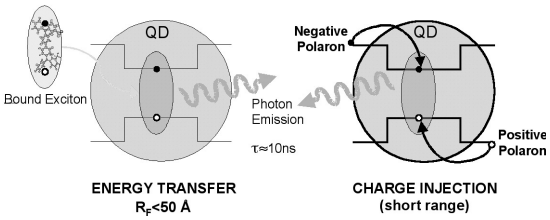

Fig. 20: Excited states of QDs can be generated by either direct charge injection or exciton transfer from an organic material. Determining the relative importance of the two processes will be essential in optimizing QD-LEDs

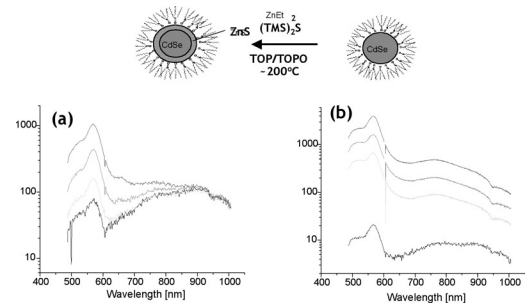

Fig. 21: Electroluminescence spectra as a function of current of HOI-LED with structure drawn in the inset of Fig. 1 and containing (a) ZnS coated CdSe nanodots and (b) uncoated CdSe nanodots. Current increases from 0.1 to 2 mA from the bottom to the top of both plots

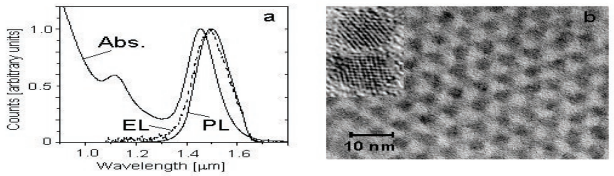

Fig. 22: Electroluminescence spectra from the visible to the near infrared of (left) CdSe and (right) PbSe based QD-LEDs.

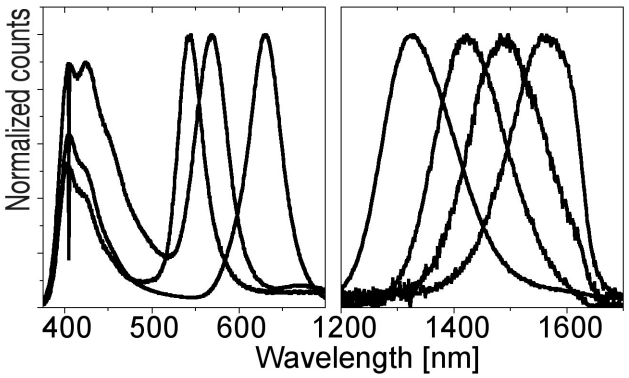

Fig. 23: (a) Typical absorption (peak at 1.456 μm), photoluminescence (peak at 1.500 μm), and electroluminescence spectra (peak at 1.495 μm) of 5.0±0.5 nm diameter PbSe particles; (b) HRTEM Image of 4.0±0.5 nm diameter PbSe particles with two enlarged images (inset).

Fast On-Chip Control Circuitry

Personnel

D. S. Crankshaw, J. Habif, and D. Nakada (T. P. Orlando, M. Feldman, M. Bocko, K. Berggren, and W. Oliver)

Sponsorship

ARO and Department of Defense University Research Initiative on Nanotechnology

RSFQ (Rapid Single Flux Quantum) electronics can provide digital circuitry which operates at speeds ranging from 1 - 100 GHz. It uses a voltage pulse to indicate a 1, and the lack of a voltage pulse within a clock cycle indicates a 0. If these electronics can be integrated onto the same chip as the qubit, complicated control with precise timing can be applied to the qubit by on-chip elements. The following design is currently in fabrication.

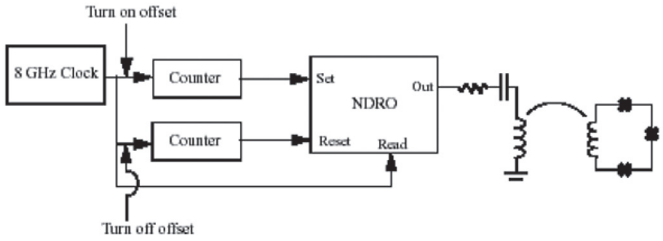

Fig. 24: An RSFQ Variable Duty Cycle Oscillator.

An RSFQ clock can be used as the oscillator to rotate the PC qubit. This oscillator has more frequency components and less tunability than a dc SQUID, but it is easier to use in conjunction with other RSFQ components. In the following design, these components can deliver a variable frequency signal (See Figure 24). An RSFQ clock is simply a Josephson Transmission Line ring. The transmission line propagates a pulse in its loop, which can be tapped off and used as a clock signal. Two counters and a Non-Destructive Read Out (NDRO) memory cell make up the digital pulse width modulator. The signal from the clock goes to both counters and to the Read input of the NDRO. The NDRO outputs a 1 for each clock input if a 1 is stored in it, but no output for each pulse if a 0 is stored in it. The output of the counters go to the Set (which sets the NDRO to 1) and the Reset (which resets the NDRO to 0) inputs of the NDRO. The counters are equal in length (13 bits), so that after 213 pulses, each one sends its output to the NDRO. By initially offsetting the counters by preloading them with the Offset inputs, one can set them out-of-phase with one another, thus controlling the duty cycle of the NDRO output. Since the NDRO signal has lots of harmonics, an RLC resonance filters the signal before delivering it to the qubit. The resonance filter converts the highly non-linear clock signal to a nearly sinusoidal signal.

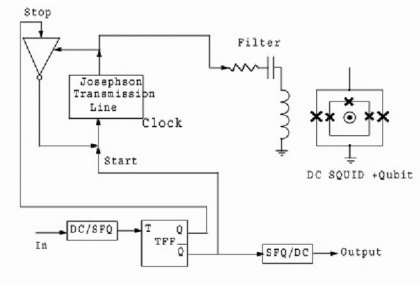

Fig. 25: An RSFQ oscillator which may be turned on and off by an external signal.

The design has been fabricated, although testing is not yet complete. The most likely difficulty is easily identified given the results presented in Sections 2 and 3. Both the RSFQ circuit and the qubit have been fabricated at a current density of 500 A/cm2, where the qubit does not display the desired quantum properties. A new design is needed for 100 A/ cm2, which is where the qubit parameters are more ameliatory. This is shown in Figure 5. This design is simpler, since 100 A/cm2 requires larger junction and inductor sizes, which lessens circuit density and it operates more slowly. In this case, the timing is done off-chip, which is beneficial for synchronizing the measurement with the driving. The oscillator is once again a Josephson transmission line ring, this time operating at 3 GHz, and a signal is tapped off to drive the qubit.

This time there is no intervening circuitry, so the qubit sees an oscillating signal as long as the clock is on. The clock is interrupted by a NOT gate. Every time the clock ring sends its signal to the NOT gate, it will send a signal back into the ring unless it has received an external signal, in which case it will not output a pulse, and the clock will turn off. The signal which stops the clock comes from off the chip, using a single T-flip-flop as a divider. The first signal which comes from off-chip will be sent by the T-flip-flop to start the clock, while the second signal will be sent to stop it.

Exciton Physics in Organic Optoelectronics

Personnel
C. Madigan (V. Bulovic)

Sponsorship
National Science Foundation CAREER Award, National Defense Science and Engineering Graduate Fellowship (DOD)

Over the last decade, enormous strides have been made in the field of organic optoelectronic devices. A first generation of visible organic light emitting devices has been commercialized. Optically pumped lasers have been demonstrated at UV, visible, and IR wavelengths. Groups have fabricated photodetectors with collection efficiencies as high as 75%, and solar cells with power conversion efficiencies as high as 3% have been reported.

As a whole, these results represent an extraordinary technological achievement, but often lost in this torrential development of new devices has been a complete physical understanding of their operation. Specifically, the factors determining the properties and behavior of molecular excitons, the fundamental excitation operating in all organic optoelectronic devices, are only imprecisely understood. In this project, we study the influence of disorder in amorphous molecular organic materials on the excitonic energy structure of constituent molecules. We highlight two excitonic processes which are general to all amorphous organic thin film structures and which strongly determine organic device operation.

(a) Solid State Solvation

Emission and absorption spectra of many organic dyes in *liquid solutions* depend on the local electric fields generated by the surrounding polar solvent molecules and the response of the electronic charge on the solvent molecules to the excitation dynamics of the solute. This "solvation effect" is a result of intermolecular solute-solvent interaction forces (such as dipole-dipole or dipole-induced dipole) that tend to stretch molecular bonds and shift charge distribution on molecules, altering the energy difference between the ground and excited states of the solute. Our earlier experiments [Bulović, *et al.*, Chem. Phys. Lett. 287 (1998) 455; 308 (1999) 317] suggested that the solvation effect is also present in *molecular solids* where closely packed polar molecules can generate large local electric fields. In these first studies, we examined the Solid State Solvation (SSS) induced luminescence red shifts of amorphous organic thin films doped with the red laser dye [2-methyl-6-[2-~(2,3,6,7-tetrahydro-1H, 5H-benzo [i,j] quinolizin-9-yl)-ethenyl]-4H-pyran-4-ylidene] propane-dinitrile (DCM2). By changing the concentration of DCM2 present in a film of N,N'-diphenyl-N,N'-bis(3-methylphenyl)-[1,1'-biphenyl]-4,4'-diamine (TPD) from 0.9% to 11%, the peak electroluminescence emission wavelength shifted from λ=570 nm to λ=645 nm (see Figure 26). (In these measurements, the DCM2:TPD film comprised the active layer of an OLED.) Because DCM2 is a highly polar molecule (with μ~11 D in ground state), and TPD is nearly nonpolar (with μ~1 D in ground state), increasing the DCM2 concentration was thought to increase the strength of the local electric fields present in the film, and that this increase in the local fields was the cause of the spectral shift. The authors viewed the mechanism as a solid state realization of solvation, and so termed it "Solid State Solvation." Similar results were also observed for DCM2 in aluminum tris-(8-hydroxyquinoline) (Alq_3) and Alq_3 in TPD (see Figure 26). Further quantification of this mechanism, however, was complicated by a subsequent report which argued that as the DCM2 doping increased in these systems, the DCM2 quantum efficiency dropped, which is generally considered an indicator of dopant aggregation [Baldo *et al.*, Chem. Phys. Lett. 347 (2001) 297]. Such aggregation, by implying substantial local inhomogeneity in doping, would make it difficult to specify the environment surrounding each molecule. We, therefore, developed an alternative system in which to study the SSS phenomenon.

We prepared spun-cast films consisting of polystyrene (PS), a small concentration of the laser dye DCM2 (< 0.005% by mass), and a range of concentrations of the polar small molecule material camphoric anhydride

continued

continued

(CA). This material system was chosen so that the DCM2 concentration could be kept constant (and very low), thereby fixing (and limiting) DCM2 aggregation effects, while still allowing for the modification of the strength of the local fields in the film. We modified these fields by changing the concentration of CA, which has a large dipole moment (μ~6D in ground state) relative to its molecular weight and is optically inactive over the range of wavelengths relevant for studying the properties of DCM2. The polymer host material polystyrene was selected because it provides a transparent, non-polar background for the system.

For a fixed DCM2 concentration of 0.005%, we found that the DCM2 emission spectrum shifts continuously from 2.20 eV (563 nm) to 2.05 eV (605 nm) for CA concentrations ranging from 0% to 25% (See Figure 27). We also performed the same measurements on films with DCM2 concentrations up to 0.05%, and observed no change in the results, demonstrating that aggregation does not play a role. Measurement of the electronic susceptibility of the films (See Figure 27) shows a marked increase with CA concentration, following a linear relationship given by A=2.44+0.13 (CA%).

Our results show that the DCM2 emission red shifts as the concentration of dipoles (i.e. CA molecules) increases in the film, and that this phenomenon is not related to DCM2 aggregation, but is consistent with the SSS mechanism sketched in Figure 28. By employing a system free of aggregation and then measuring the electronic susceptibility, however, we can take the model a step further and apply the theory of liquid solvation quantitatively to our films.

Using the Ooshika-Lippert-Matanga (OLM) approach [Ooshika, *J. Phys. Soc. Japan*, 9 (1954), 594; Lippert, *Z. Naturforsch.*, 10a (1955), 541; Mataga *et al.*, *Bull. Chem. Soc. Japan*, 29 (1956), 465.], we may write for the relaxation energy under the influence of solvation from a dielectric medium as,

(1) $$E^{\downarrow} = C - A\ddot{E}$$

where

(2) $$\ddot{E} \equiv \frac{2(\breve{a}-1)}{2\breve{a}+1}$$

and A and C are constants. In Figure 29, we plot three different fits to the spectral data, indicating the sensitivity of the fit to the choice of A. We find that the trend in the spectral shift is in excellent agreement with the solvation theory, with the optimal fit obtained for A = 0.57 eV.

It is difficult to determine how plausible this value is based on the definition for A because of inherent arbitrariness in the specification of the OLM parameters. However, we *can* look at solvation in solutions where the solvation mechanism is known to operate. A plot of the peak emission energy for DCM2 in different solvents is shown in Figure 29 against each solvent's value for ε. We find that the OLM theory again works quite well and obtain an optimal fit for A = 0.55 eV.

The SSS mechanism can, therefore, comprehensively describe the observed spectral shifts, and the model parameter is consistent with known values for DCM2 in solution. A priori, this result is not surprising as one could argue that dielectric relaxation in amorphous organic solids should be similar to that of liquids. Indeed, the SSS process can strongly determine the dispersion and position of molecular energy levels in organic solids. Additionally, SSS could be used as a new method for the engineering of energy structures, both for excitonic levels (as studied in this work) and for conduction levels (which are also subject to solvation).

continued

continued

(b) Exciton Diffusion

The second process we have studied is Exciton Diffusion which refers to the migration of excitons between molecules. Though the presence of exciton diffusion is well-known, the details of the phenomenon have not been studied in a disordered solid. Specifically, the impact on this process of dispersion in molecular energy levels has been previously ignored, but we find plays a controlling role.

Time resolved photoluminescence measurements of disordered molecular organic thin films of Alq_3 doped with DCM2 show an emission spectrum that significantly red shifts as a function of time following excitation by a 100 fs laser pulse (See Figure 30). (The spectral measurements were performed using a Hamamatsu streak camera.) Spectral shifts of ~ 0.10 eV over a time window of ~ 10 ns are observed for doping levels ranging between 0.5% and 5% in addition to significant spectral narrowing over that same period. We show that this previously unreported phenomenon can be attributed to the diffusion of excitons through the film by means of Forster energy transfer between DCM2 molecules.

This site-to-site transfer rate is governed by the emission and absorption spectra of the exciton donating and the exciton accepting molecule. From Förster's original formulation, the rate of exciton transfer, $\tilde{A}_F$, is given as

$$\tilde{A}_F = \frac{1}{\hat{o}_{rad}} \left(\frac{R_F}{R} \right)^6 \qquad (3)$$

where R is the distance separating the donor and acceptor, $\hat{o}_{rad}$ is the intrinsic radiative lifetime of the donor, and R_F is the Förster radius, given by,

$$R_F = \frac{3\, c^4}{4\delta\, n^4}\, \acute{e}^2 \int \qquad (4)$$

where $\acute{I}^2$ reflects the relative orientation of the donor and acceptor, n is the index of refraction of the medium, S_p is the normalized donor fluorescence spectrum, and $\acute{U}_A$ is the acceptor molar absorption cross section (in units of cm^2).

As indicated by the rate expression, the Förster energy transfer occurs more readily when the acceptor molecule has lower energy spectra than the donor. In other words, the Förster mechanism preferentially transfers excitons towards lower energy sites. If we combine this observation with an assumption that the excitonic density of states, $g_{ex}(E)$, has a non-zero width (i.e. that there exists some dispersion in exciton energies in our film), we obtain a straightforward explanation of the observed time-resolved spectral shifts: diffusion by Förster energy transfer progressively drives the excitons in the film towards the lowest energy sites.

We developed a Monte Carlo simulation of this diffusion process. The simulation tracks the emission and Förster energy transfer of excitons in a large lattice of molecular sites, with each site characterized by its position and peak emission energy. The lattice spacing corresponds to the mean molecular inter-site spacing. The histogram of all the site energies reproduces the shape of the $g_{ex}(E)$ distribution. We have assumed that $g_{ex}(E)$ has a Gaussian form, with a full-width-half-max (FWHM) of w_{DOS}. Once the system of sites has been created, each site is populated with an exciton, yielding an exciton population, $n_{ex}(E,t)$, such that,

$$n_{ex}(E,t=0) \propto g_{ex}(E) \qquad (5)$$

where t=0 refers to the time immediately following the arrival of the PL excitation pulse. Then for each time step of length U_{step} each exciton has the opportunity to Förster transfer to another site or to emit.
The simulation yields results consistent with the experimentally observed shifts (See fits in Figure

continued

continued

30), and through fitting of the available parameters, provides a probe of w_{DOS} and R_F. The values for w_{DOS} decrease from ~0.260 eV for 0.5% DCM2 doping to ~0.205 eV for 5% doping. In addition we find that R_F falls with increasing doping, from 38 Å for 0.5% to 20 Å for 5%. We can not turn to any published results for a direct comparison of these fitted values. However, there do exist calculations of w_{DOS} for polaron levels in amorphous organic materials, where the polaron $w_{DOS} \sim 0.1eV$. Though it is not necessary that polaron levels and excitonic levels should experience identical energy dispersion, it is reasonable to expect that they are comparably dispersed, which is what we observe.

We know of no other method for measuring the energy dispersion in exiton energies in the literature. For this reason, this technique potentially represents a major breakthrough in the analysis of energy structure in amorphous organic solids. We have also demonstrated this modeling method with neat films; we studied time-dependance of PL in films of Alq_3 and $Ir(ppy)_3$. The evolution of the peak PL for these two films is shown in Figure 31, along with fits from our simulation. Note that spectral shifts just like those observed in the DCM2:Alq_3 system are observed. In both cases, we obtain R_F ~ 12 Å and w_{DOS} ~ 0.075 eV, which, as per the arguments made above, have reasonable magnitudes. The similarity between the two systems should not be surprising as they have similar molecular ground state dipole moments and bulk spectral overlaps.

By extension, this technique should apply to any pure organic thin film material in which Förster energy transfer occurs. Experimentally, all that is required is a film with thickness of at least 20 nm and an ultrafast source operating at a wavelength for which the film is absorptive. Thus we find that this technique is not only of great value in analyzing excitonic properties in organic thin films, but its application is also straightforward and general.

(c) Conclusions

In inorganic, crystalline semiconductors, accurate physical models have been invaluable in assisting technological improvement. Currently, however, very few physical models describe electronic and excitonic behavior in organic optoelectronic devices. The larger aim of this work is the development of a practically useful model of electronic and optoelectronic processes in amorphous organic solids, which might then be used to predict the behavior of new organic device structures. The quantification of SSS helps us towards this goal in identifying one of the primary mechanisms by which solid state energy levels are altered from their gas phase values. In addition, it identifies an additional lever with which one can modify energy levels through the modification of bulk property (i.e. electronic susceptibility). The development of a more comprehensive theory of exciton diffusion aids us by providing a building block for a total model of electronic and optoelectronic processes in organic thin films. Combined with a carrier transport model and a microcavity model, one can already imagine constructing a simulation of a working OLED. And as indicated above, applying the exciton diffusion model to dynamic spectral shifts allows us to obtain previously inaccessible information about the excitonic energy level dispersion. While much work remains in developing physical models of processes in organic optoelectronic devices, these results already represent a significant step forward (See Figure 32).

continued

continued

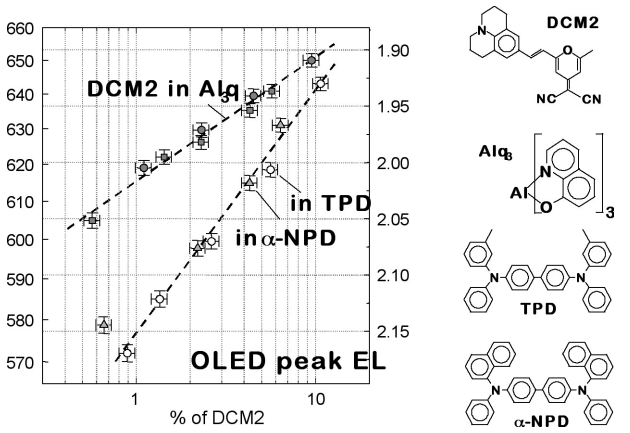

Fig. 26: (a) Evolution of peak PL spectra of DCM2 in films of Alq_3, TPD and α-NPD.; (b) chemical structures of molecules used in this work.".

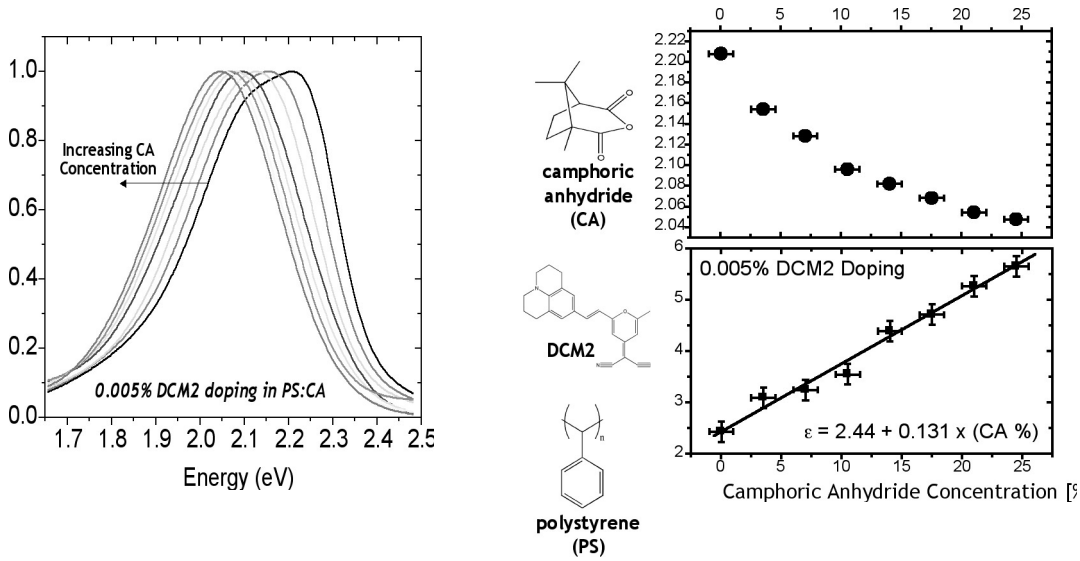

Fig. 27: (left) PL spectra of 0.005% DCM2 in PS:CA films. The spectrum red-shifts as the CA concentration is changed from 0 to 25%. (middle) Chemical structures of CA, DCM2, and PS. (right) Change of the peak luminescence energy and the dielectric constant as a function of CA doping.

continued

continued

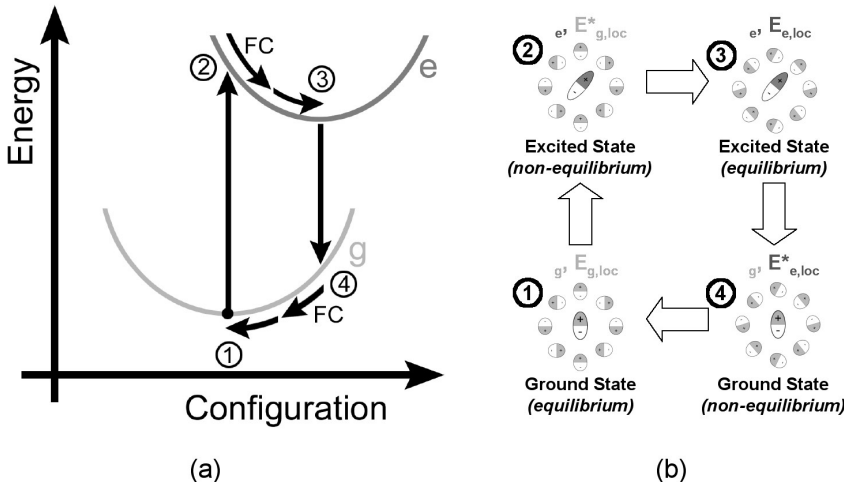

Fig. 28: Equilibrium and non-equilibrium states of the solvation process.

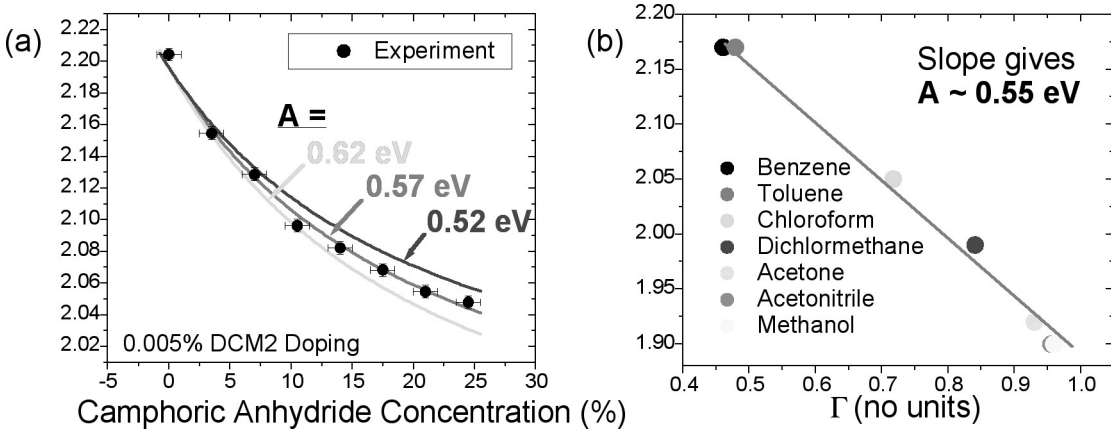

Fig. 29: (a) Fits of OLM theory to observed evolution of DCM2 peak PL energy; (b) OLM fit to DCM2 PL data in solution.

continued

continued

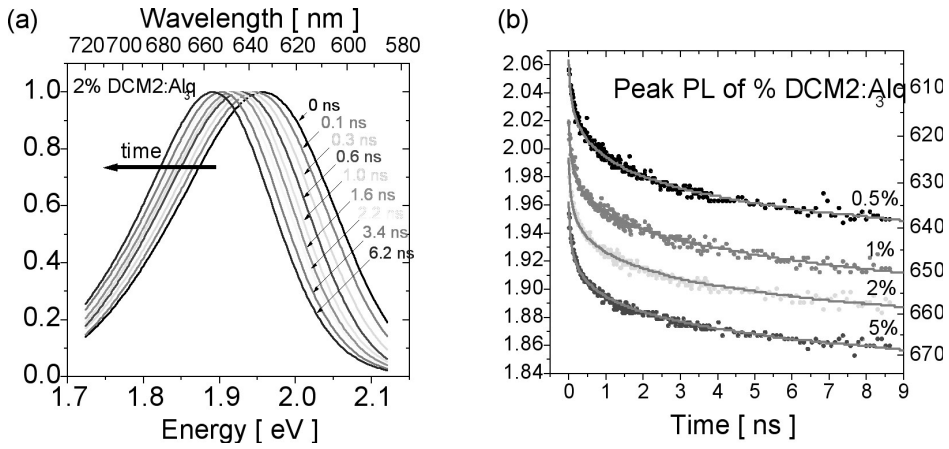

Fig. 30: (a) Normalized DCM2 PL spectra, following ultrafast excitation; (b) Evolution of peak PL of DCM2 doped in films of Alq_3. Grey lines denote simulation results optimized for each data set.

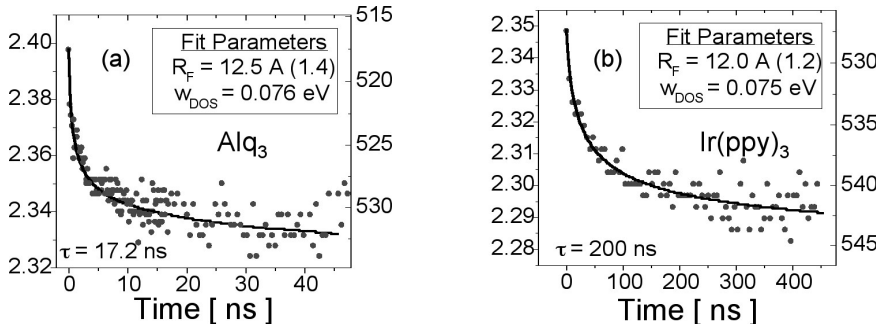

Fig. 31: (a) Evolution peak PL of Alq_3 with simulation fit; (b) evolution of peak PL of $Ir(ppy)_3$ with simulation fit.

continued

continued

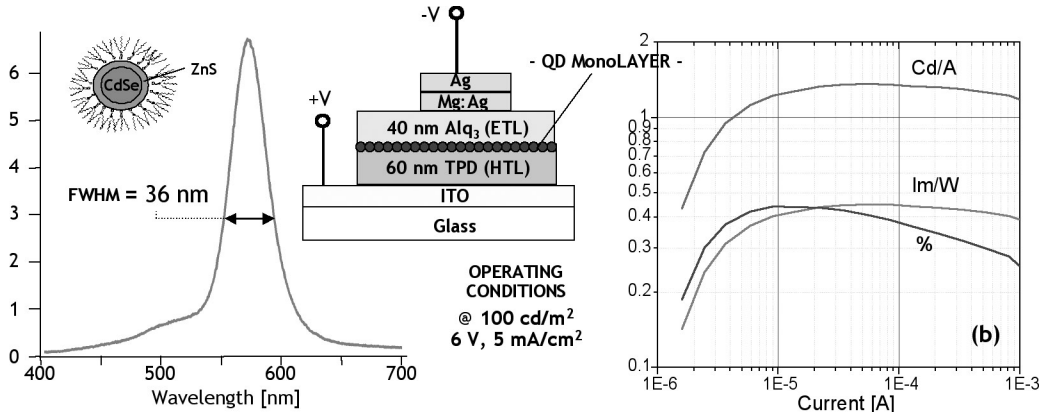

Fig. 32: Hybrid organic/inorganic light emitting device contain inorganic QDs. (Inset) QD-LED cross section. (left) Electro-luminescence spectrum at ~100 cd/m^2, with inset device cross section. (right) QD-LED quantum efficiency in percent units, and luminescence efficiency in units of Cd/A and lm/W.

Efficient Electrically Pumped Polariton Emission in a J-Aggregate OLED at Room Temperature

Personnel
J. Tischler (V. Bulovic)

Sponsorship
DARPA Optoelectronic Center for Innovative Photonic Chipscale Technologies

The goal of this project is to develop ultrafast active optoelectronic devices based on the unique physical properties of J-aggregates and their interaction with light. The essential physics of J-aggregates underpinning this project is that the excited state of a J-aggregate is a delocalized Frenkel exciton of high oscillator strength, which enables it to couple strongly to the optical field inside a resonant cavity according to the principles of semiconductor cavity QED. We are using J-aggregates because J-aggregates exhibit the strong coupling regime of Cavity QED, even at room temperature, even in an all-metal cavity, and because their lifetime is extremely short. The ultimate goal is to realize the vision of the electrically pumped polariton laser and polariton optical switches at room temperature, using J-aggregates as our material platform. The first milestone is to develop a room temperature polariton LED.

J-aggregates are ordered arrangements of highly polar cyanine dye molecules (See Figure 33) in which the transition dipole moments of the individual molecules add to form a giant dipole oscillator. When dye molecules form a J-aggregate, a new optical transition develops called a J-band. Relative to the monomer, this optical transition of the J-aggregate is red-shifted, minimally stokes shifted, and considerably narrower in energy, and the lifetime of this transition is also much faster. J-aggregates are therefore described anatomically and functionally. Anatomically, they are crystalline phase of the dye monomers, although not necessarily the lowest energy crystalline form, and functionally, they are quantum systems in which the excitons delocalize over several molecular sub-units of the aggregate, which gives rise to narrow absorption and emission spectra.

J-aggregates received their moniker in recognition of Edwin Jelly, who, while working for Kodak in the 1930's, discovered that the cyanine dye, PseudoIsoCyanine (PIC), at high concentrations became resonantly fluorescent [E. E. Jelly, Nature 138, 1009 (1936)]. This was surprising at the time because PIC at lower concentrations is not fluorescent. It is also contrary to the generally accepted rule of concentration quenching which states that the higher the concentration is, the lower the quantum yield of fluorescence. From that point forward, J-Aggregates have been studied to understand the physics of excitons, their optical properties, and their crystallographic properties; and this understanding has been fruitfully applied to the science of sensitizing photographic active silver halide crystals to narrow bands of light in regions of the visible spectrum that the silver halides would otherwise not absorb.

The genesis for our research effort has come from the recent demonstration of room temperature polariton photoluminescence from J-aggregate Frenkel excitons coupled to the cavity photon mode [Lidzey et al., Nature 395, 53 (1999)]. Because of the high oscillator strength of the Frenkel exciton, Rabi Splitting exceeding 100meV was realized, an order of magnitude larger than the splitting achieved in inorganics even at ultralow temperature. This work laid the foundation for us to start imagining how we could access the strong coupling regime using J-aggregates in active optoelectronic devices.

To make these devices, J-aggregates must be formed in a thin film process. J-aggregates can be formed in solution and in solid state. In solution, particularly in water, the dye molecules form aggregates at high concentration and in an alkaline environment; while in solid state, J-aggregates form more readily when in contact with a polymer template. In our present studies, we use PolyVinyl Alcohol (PVA) polymer layer. We have chosen JC-1 as the J-aggregate molecule (See Figure 34). JC-1 readily forms J-aggregates even at ultra low concentrations (10^{-5} M) and has been well studied

continued

continued

in the photographic industry, as a membrane potential sensitive dye, and for its rich exciton dynamics. To investigate it's applicability for strong coupling devices, we sought to demonstrate Rabi Splitting and measure the polariton dispersion curve for JC-1. We prepared a series of samples, consisting of silver mirror layer (1200Å), J-Aggregate/PVA matrix and a thin silver film on top (300Å) (See Figure 35). The thickness of the J-Aggregate layer was varied so as to tune the bare cavity mode through the J-Aggregate exciton resonance. From reflectivity measurements taken from 7° - 70°, we conclude that JC-1 does in fact exhibit a strong coupling to the photon mode as illustrated by the anti-crossing in the dispersion curves. From this data and other dispersion curves we calculate a Rabi Splitting of >95 meV.

Our current objective is to develop an efficient J-Aggregate OLED that we can then fabricate within an optical cavity to demonstrate electrically pumped polarition emission. Presently, we have successfully demonstrated EL from JC-1 in an exploratory structure consisting of a mixed film of PVA doped with JC-1 (See Figure 36).

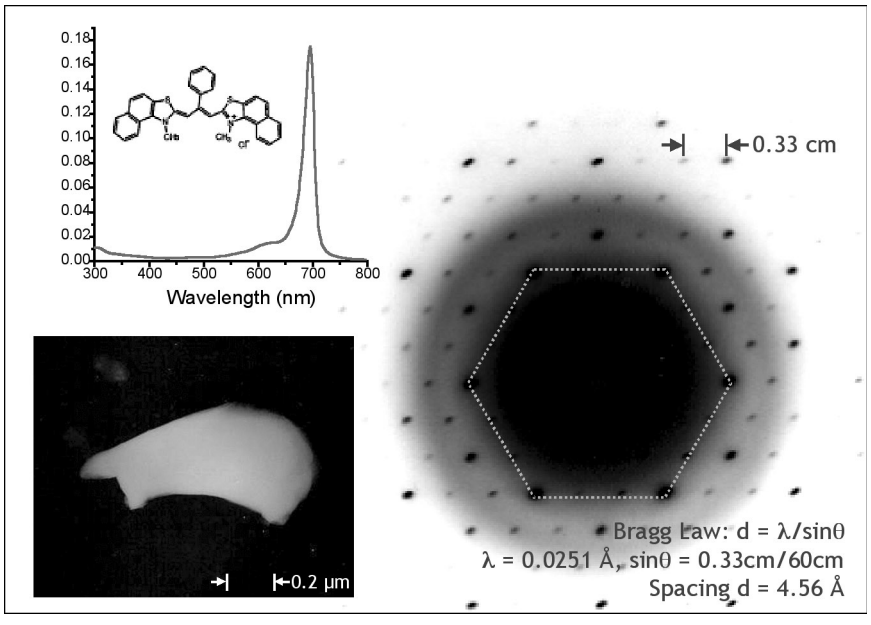

Fig. 33: Absorption spectrum, TEM Micrograph, and electron diffraction pattern of a J-aggregate dispersed in polyvinyl alcohol.

continued

continued

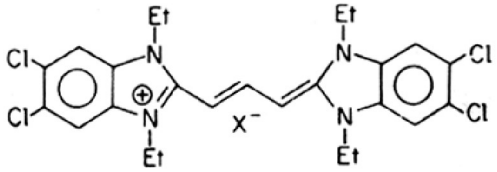

Fig. 34: JC-1, a cyanine dye that readily forms J-aggregates in solution and solid state.

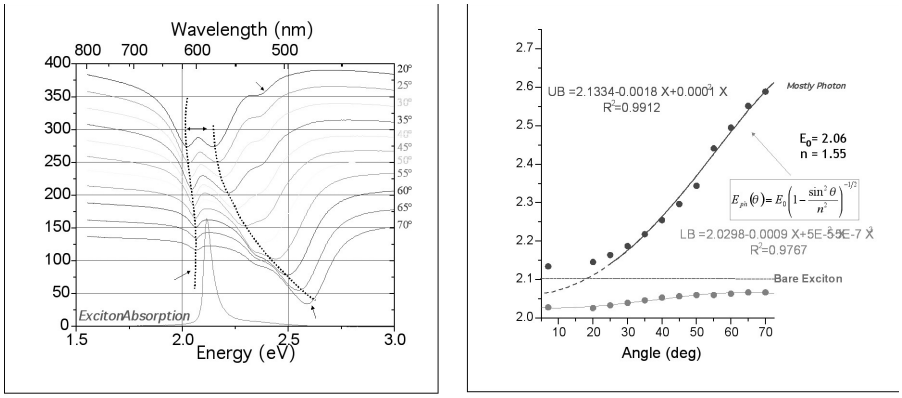

Fig. 35: Angle dependent reflectivity and dispersion curve of a silver mirror metal microcavity containing J-aggregates of JC-1 in polyvinyl alcohol.

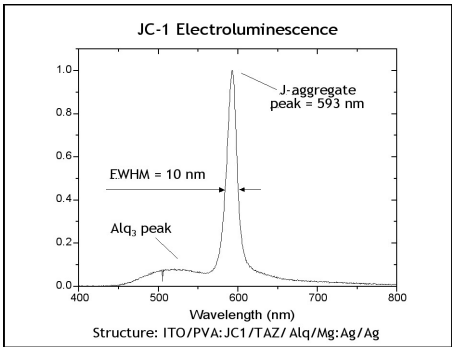

Fig. 36: Electroluminescence spectrum of a JC-1 OLED.

An On-Chip Frequency-Domain Submillimeter-Wave Spectrometer

Personnel
J. Montoya (Q. Hu)

Sponsorship
Rosenblith Fellowship

Because of the frequency limitation of semiconductor electronic devices, measurement instruments such as network analyzers can operate only below approximately 100 GHz. Thus, even if ultrahigh-frequency HBTs can be developed, they can only be directly measured up to 100 GHz, with higher-frequency performance extrapolated according to certain frequency roll-off models. Clearly, such an extrapolated measurement will not be applicable to measuring high-frequency resonance such as that shown in Figure 37. It will be very useful to develop on-chip systems that can characterize device performance up to THz frequencies. A promising component for such systems is ultrafast photoconductive switches made of Low-Temperature-Grown (LTG) GaAs materials. When pumped with two coherent laser beams, such switches can generate and detect photocurrent with a modulation frequency beyond one THz.

Furthermore, photoconductive emitters and receivers are attractive as components of sub-millimeter-wave spectroscopy systems because of their tunability, compactness, and ability to be monolithically integrated with antennas, transmission lines, and microelectronic devices. Such systems can be classified either as time-domain or frequency-domain systems. Time-domain systems, which contain a photoconductive pulse emitter and sampler excited by a mode-locked laser, are the most investigated. They have been used for free-space characterization of semiconductor materials, and on-chip characterization of ultrafast devices and circuits with 2.7 ps time resolution. The frequency resolution is the inverse of the time span over which the propagating pulse is sampled. This span is determined by the length of an optical delay line, which usually results in a frequency resolution broader than 1 GHz.

The emitter and receiver of a frequency-domain spectrometer will be pumped by two coherent cw laser beams with frequencies ω_1 and ω_2, instead of short laser pulses. If the response time is sufficiently fast, the emitter switch will generate an ac photocurrent with a frequency $|\omega_2-\omega_1|$ which can easily exceed 1 THz. Illuminated by the same two laser beams with a controlled delay, the receiver switch can be used to perform a homodyne detection of the ac photocurrent generated from the emitter. In combination with high-frequency transmission lines, they can form on-chip spectrometers with THz bandwidths. Figure 37 illustrates a schematic of such a spectrometer that can be used to characterize common-emitter performance of high-frequency HBTs.

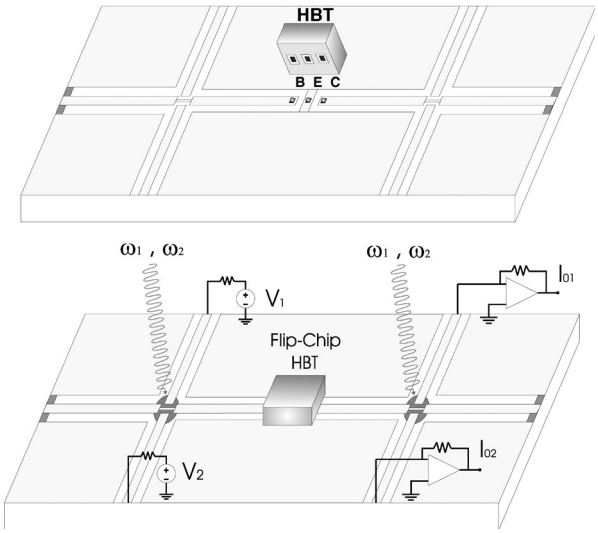

Fig. 37: Schematic of a on-chip spectrometer that uses ultrafast photoconductive switches to generate and detect ultrahigh-frequency signals.

Because of the broad bandwidth (>1 THz) and a high frequency resolution (better than 1 MHz), such a spectrometer is also adequate for molecular line spectroscopy. In combination with microchambers, the spectrometer can be part of a microfluidic, "lab on a chip"-type circuit which can be used as on-chip sensors for chemical and biological agents. As the first step

continued

in the development of an on-chip frequency-domain spectrometer, we have investigated the performance of an on-chip transceiver containing only uninterrupted CoPlanar Waveguides (CPWs).

In order to improve the coupling efficiency of the photoconductive switches and to reduce their RC time constants, we used interdigited finger electrodes fabricated using e-beam lithography. A SEM picture of such a photoconductive switch is shown in Figure 38.

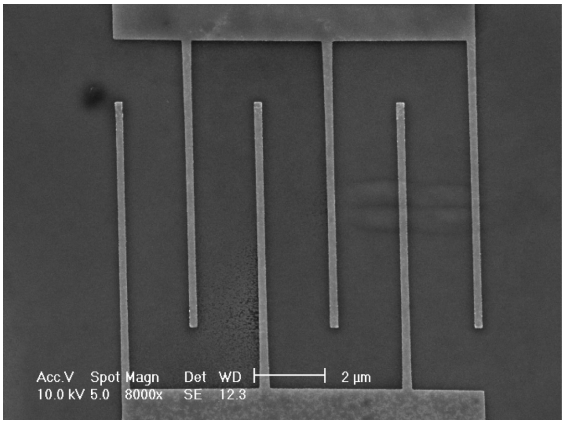

Fig. 38: SEM picture of a photoconductive switch with interdigited finger geometry and fabricated using e-beam lithography.

Previously, we have shown that LTG-GaAs photoconductive switches embedded in a transmission line can function as an intensity-intensity autocorrelator, based on the nonlinearity of a voltage divider including the photoconductive switch and the characteristic impedance of the transmission line. The time resolution of this autocorrelator, however, is limited by the response time of the LTG-GaAs photoconductive switch, which is on the order of 1 ps. In order to improve the time resolution of the autocorrelator to the degree that it can resolve the time span of femtosecond laser pulses, a more intrinsic nonlinear process must be used than the voltage divider scheme. In a recent experiment, we have developed a much faster autocorrelator by using two-photon absorption process in the photoconductive switch. The almost instantaneous nature of this nonlinear process greatly improves the time resolution of the autocorrelators. Figure 39 shows the measured time profile of fs laser pulses from a mode-locked Ti:sapphire at 900-nm wavelength. At this long wavelength, the photon energy is smaller than the energy gap of LTG-GaAs; thus, single photon absorption is suppressed. As can be seen from Figure 39, the pulse shape measured using this novel autocorrelator is in good agreement with that measured using a conventional autocorrelator with SHG crystals. This development could lead to compact, alignment free autocorrelators with femtosecond time resolutions. Furthermore, the gap energy of LTG-GaAs will make it a natural candidate for the two photon absorption measurements at ~1500-nm wavelength, which is important for fiber telecommunications.

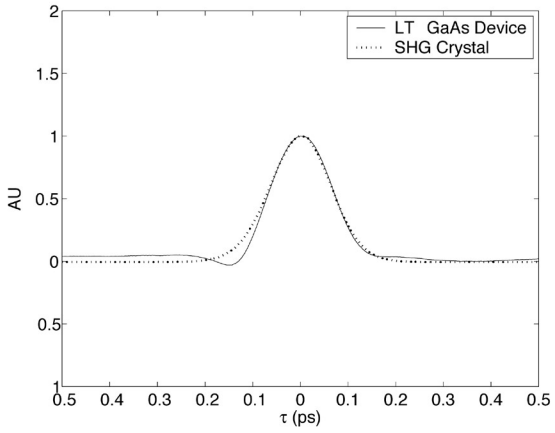

Fig. 39: Two photon absorption autocorrelation at 900-nm wavelength with an average laser power of 170 mW.

Measurement of Qubit States with SQUID Inductance

Personnel
J. C. Lee (T. P. Orlando and W. Oliver)

Sponsorship
AFOSR/DURINT, ARDA, and NSF

For the persistent current qubits, the two logical states correspond to currents circulating in opposite directions. The circulating current generates a magnetic flux that can be sensed by a SQUID magnetometer inductively coupled to the qubit. Depending on the state of the qubit which determines the direction of the persistent current, this additional flux either adds to or subtract from the background magnetic flux. Therefore, during the readout process, the two qubit states can be distinguished by a difference in magnetic flux signal, typically on the order of a thousandth of a flux quantum.

It is of great consequence that the measurement setup has minimum back-actions on the qubit. The present measurement scheme is the so-called switching current method and has some major drawbacks. It uses the property that the critical current of a SQUID is a function of the magnetic flux that it senses, and hence, will be different depending on what state the qubit is in. During the measurement, the value of the critical current is obtained directly by ramping a DC current through the SQUID and determining the point at which it switches from the superconducting state to the finite voltage state. This method requires a high current bias and introduces severe back-actions on the qubit.

The SQUID inductance measurement scheme was proposed to be an improvement over the switching current method. With this method, the current through the SQUID can now be biased significantly below the critical current level, and hence, reduces the back-actions on the qubit. The idea is to use the SQUID as a flux-sensitive inductor. Basically, the Josephson inductance across the junctions of the SQUID is also a function of the magnetic flux. To measure the inductance effectively, the SQUID is inserted in a high Q resonant circuit (See Figure 40). Note that the circuit is fed by a DC current bias as well as an AC source of a single frequency ω_b.

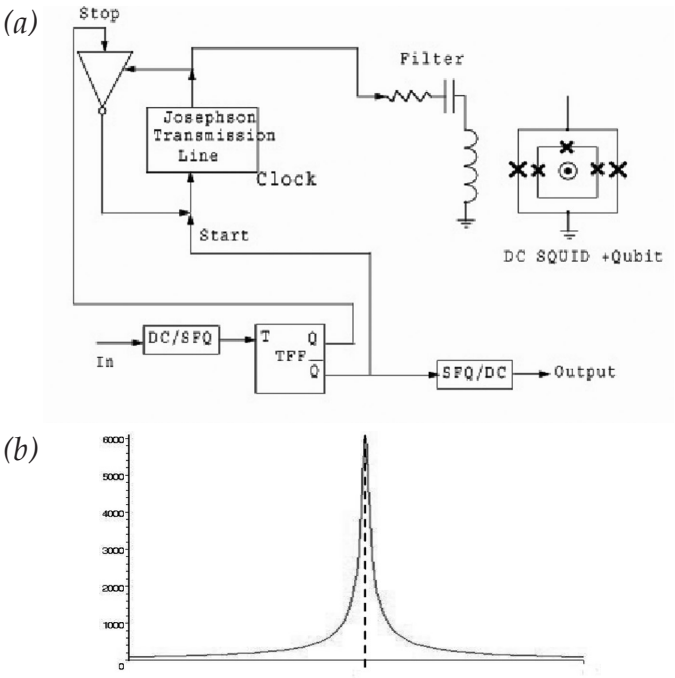

Fig. 40: (a) A resonant circuit used to measure the SQUID inductance. The 'x' represents a Josephson junction. This circuit is simplified from the actual design for illustrative purpose. (b) The corresponding plot of the magnitude of the impedance vs. frequency. The resonant frequency is denoted as ω_o.

Upon a change in the qubit state, the corresponding change in the SQUID inductance will shift the resonant frequency (See Figure 41). This is because the resonant frequency is given by $1/\sqrt{LC}$, where L is the inductance of the SQUID. If one keeps the AC current source at a bias frequency £sb, typically around 500MHz, one senses a change in the impedance ΔZ. This in turn results in a difference in the output voltage ΔV corresponding to $I_{AC} X \Delta Z$. This voltage difference will be measured to detect the state of the qubit.

continued

continued

High Q resonant circuits were designed with impedance transformation and impedance matching techniques to optimize the measurement process. Detailed calculations were performed for the specific circuits currently being fabricated at the MIT Lincoln Laboratory, and the voltage corresponding to the qubit signal is expected to be about 10μV.

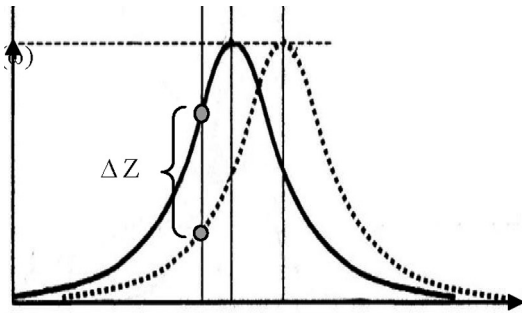

Fig. 41: Illustration of the shift in resonant frequency $\Delta\omega_0$ upon a change in the qubit state. During the measurement, one biases the operating frequency at £sb and senses a change in impedance ΔZ, which in turn can be retrieved as a voltage signal.